



City Research Online

City, University of London Institutional Repository

Citation: Riziotis, V. A., Katsaounis, G. M., Papadakis, G., Voutsinas, S. G., Bergeles, G. & Tzabiras, G. D. (2013). Numerical and experimental analysis of the hydroelastic behavior of purse seine nets. *Ocean Engineering*, 58, pp. 88-105. doi: 10.1016/j.oceaneng.2012.09.022

This is the accepted version of the paper.

This version of the publication may differ from the final published version.

Permanent repository link: <https://openaccess.city.ac.uk/id/eprint/14852/>

Link to published version: <https://doi.org/10.1016/j.oceaneng.2012.09.022>

Copyright: City Research Online aims to make research outputs of City, University of London available to a wider audience. Copyright and Moral Rights remain with the author(s) and/or copyright holders. URLs from City Research Online may be freely distributed and linked to.

Reuse: Copies of full items can be used for personal research or study, educational, or not-for-profit purposes without prior permission or charge. Provided that the authors, title and full bibliographic details are credited, a hyperlink and/or URL is given for the original metadata page and the content is not changed in any way.

City Research Online:

<http://openaccess.city.ac.uk/>

publications@city.ac.uk

Numerical and experimental analysis of the hydroelastic behaviour of purse seine nets

V. A. Riziotis^{a,*}, G.M. Katsaounis^b, G. Papadakis^a, S.G. Voutsinas^a, G. Bergeles^a and G.D. Tzabiras^b

^a School of Mechanical Engineering, National Technical University of Athens, 9 Heron Polytechniou str., GR15780, Athens, Greece.

^b School of Naval Architecture and Marine Engineering, National Technical University of Athens, 9 Heron Polytechniou str., GR15780, Athens, Greece.

* Corresponding Author. Tel: +30210 7721101, Fax: +3210 7721057, e-mail: vasilis@fluid.mech.ntua.gr

Abstract.

The paper presents a general three dimensional hydro-elastic tool for the analysis of different types of fishing nets and aquaculture facilities. Flexible net strands are modeled by non linear truss elements having two nodes. Hydrodynamic loads due to relative motion of the net with the surrounding fluid are computed using Morison equation. The coupled hydrodynamic-elastodynamic equations are solved using finite element (FE) approximations. Furthermore, experimental data are presented for the drag resistance of a purse seine net, commonly used as fishing tool in the Mediterranean sea. The measurements were conducted in the towing tank of NTUA on a sample of a net. The net was tested in three configurations: vertical, horizontal and inclined at 45°. The derived drag coefficients are compared to predictions of the FEM developed model. The vertical submergence behavior of the seine in calm water is also examined, both experimentally and theoretically. Moreover, the shooting phase of the purse-seine fishing is simulated with the aim to investigate the diving behavior of the net. The flow shading effect of neighboring strands is identified as a critical parameter for the consistent predictions of the diving behavior.

Keywords: fishing nets, hydroelasticity, finite element, truss elements, hydrodynamic loading

1. Introduction

Purse seining is a traditional fishing method commonly used in the Mediterranean Sea. It is appropriate for fishing pelagic fishes or other species, swimming in dense groups (schools) near the

sea surface. A typical purse seine, shown in Figure 1, is composed by (a) a lacing rope at the top, bearing distributed floaters, (b) the net itself, and (c) the lower rope, running along the bottom edge and having distributed lead weights (sinkers) which serve submersion. The rope is linked via rings (pursing rings) to a pursing wire. The mesh of the seine, usually of diamond type, has a size that varies depending on the aimed species. Fishing starts by setting the head floater and deploying the net, encircling a herd of fish. During the shooting phase the net submerges by the action of the sinkers and, eventually, impounds the fish. At closing the circle the pursing process begins. The pursing wire is being tightened, giving a purse-like shape to the seine (Figure 2). The hauling phase follows and the net with the fish is led aboard.

An important parameter of the shooting phase is the depth reached by the net during the circular motion of the trawl. If the depth reached is too low the herd may escape. On the other hand, reaching ground during net deployment may cause serious damages to the ecosystem of the sea bed, apart from the inevitable destruction of the seine itself. In order to prevent environmental disasters, authorities have issued pertinent regulations [European Union, 2006], applying restrictions on the fishing areas and controlling the drop (height) of the net according to the depth of the fishing area. Evidently, the drop to depth ratio is not the only parameter influencing the grounding of the seine. In fact, due to the influence of the currents, the method of deployment and the action of waves, the submerging speed is actually so small that, regardless of the net height, the boat can draw a small or medium circle, set the seine and start pursing, before the net reaches the sea bed.

The analysis of the static and dynamic behavior of the seine should be based on reliable drag resistance estimations. Drag force dominates the hydrodynamic loading of a net subjected to sea currents or moving in still water. The determination of the normal and tangential forces can be achieved either by examining the local to the twines flow [see Morison et al, 1950 and Løland, 1993] and obtaining values corresponding to the local Reynolds number, or by using averaged global values for a larger portion of the net, based on experiments. In the latter case Kawakami (1959 and 1964) among others, studied analytically the resistance to currents and proposed simple formulae for the drag coefficient. Aarsnes et al. (1990) carried out tests on net panels and cage systems and developed formulae for drag and lift forces due to constant current. In his analysis, Aarsnes considered also the effect of the flow direction. Zhan et al (2006) derived expressions for the drag coefficient that depend on the solidity ratio of the net and examined experimentally the effect of Reynolds number, mesh pattern and flow direction on the drag force of planar and circular nets.

In the modeling of fishing nets or other aquaculture systems like net cages, two main groups of structural dynamics analysis methods are found in the literature. In the first group the twines of the net are considered as rigid bars [see Bessonneau and Marichal, 1998] or lumped masses connected through concentrated springs [see Lee et al, 2005 and Shimizu et al, 2005], or truss elements exhibiting linear or non linear elastic behavior [see Gignoux and Messier, 1999, Tsukrov et al, 2003 and DeCew et al 2010]. In the latter case the net system is treated numerically in the context of finite element method (FEM). In this group of methods the hydrodynamic loading is determined by examining the local to the twine flow. Usually Morison equation is applied in the calculation of the normal and tangential loads while naturally hydrodynamic added mass contribution is accounted for. Since the number of cells of the actual net is too big, mesh mapping methods have been devised, in order to retain computational cost at reasonable levels. Following such methods, equivalent less dense meshes are defined that resemble the actual net in terms of hydrodynamic loading [Gignoux and Messier, 1999 and Tsukrov et al, 2003].

The second approach is to model the net by dividing it into planar four side super-elements, where each element has properties (inertial and structural) that simulate the twine and the knot structure of the netting [Lader and Fredheim, 2006 and Chuang et al, 2006]. The nodes of the super-element are connected with springs having stiffness calibrated on the basis of tensile-tests, carried out on a sample of the net. The hydrodynamic loads on the whole net element (and not the individual twine) is separated into drag and lift components, which can be calculated using global force coefficients that depend on the solidity and Reynolds number, like those proposed by Aarnes et al (1990) and Zhan et al (2006).

All the above mentioned methods have been extensively applied to the modeling of several types of nets, like trawling nets [Bessonneau and Marichal, 1998], purse seine nets [Lee et al, 2005] and net cages [Tsukrov et al, 2003] and they have been validated against measurements and in situ observations in towing tanks [Lader and Enerhaug, 2005] or in ocean environment [Shimizu et al, 2005].

Herein a general, three dimensional hydro-elastic tool for the analysis of different types of fishing nets is presented. Flexible net strands are modeled by two noded non linear truss elements, applying the tangent stiffness matrix approach [see Crisfield, 1991]. Hydrodynamic loads due to relative motion of the net with the surrounding fluid are computed using Morison equation. Consistent equivalent nets are defined which retain both the drag and the inertia properties of the real net. Hydrodynamic load

coefficients have been corrected based on resistance tests performed at NTUA's towing tank by Katsaounis et al (2009), in order to account for the flow shading effect caused by upstream strands. The vertical submergence behavior of a seine in still water is examined, both using the FEM tool but also experimentally by means of submergence tests performed at NTUA. In situ observations are compared to the predictions of the tool as well as to the predictions of a simplified one dimensional non-elastic net model that reproduces the basic mechanics of the submerging system. A good agreement of the predictions of the FEM code with the submergence test observations is obtained if consistent correction is made to the drag of the submerging net, in order to account for the interaction of the strands. Moreover, the shooting phase of the purse-seine fishing is simulated with the aim to investigate the diving behavior of the real net.

2. The numerical model

A consistent 3D model of the net is developed, in which the structural dynamic behavior of the net is modeled using finite element method. Hydrodynamic loading on the net, due to the relative motion of the net twines in the surrounding fluid, is calculated by means of Morison equation. Consistent equivalent net panels retaining the projected area and mass of the actual net are defined.

2.1 Finite-element analysis of fishing nets

Prediction of the hydro-elastic response of fishing nets is performed on the basis of finite element analysis. The twines of the fishing net are represented by truss elements exhibiting a non linear elastic behavior. Such elements transfer only the tensile forces while their compression stiffness is zero.

In Figure 3 a truss element P_0Q_0 of initial undeformed length $\ell_0 = 2\alpha_0$ is shown. The non-dimensional coordinate ξ (ranging from -1 to 1) is used to define the arbitrary point R_0 along the element. The position vector of this point initially is \mathbf{r}_0 . As a result of rigid body motion and elastic deformation the truss element will move to a new position P_nQ_n . The arbitrary point along the element (point R_n) will now have a position vector \mathbf{r}_n given by the following expression:

$$\mathbf{r}_n = \mathbf{r}_0 + \mathbf{u} \quad (1)$$

where vector \mathbf{u} represents displacement due to elastic deflection and rigid body motion of the element.

Applying the virtual work principle [see Crisfield, 1991] the dynamic equations of a truss element in space are obtained. The principle requires that, for an arbitrary virtual displacement field $\delta\mathbf{u}$:

$$\int_{V_0} \sigma \delta\varepsilon dV - \int_{\ell_0} \delta\mathbf{u}^T (\mathbf{q}^e - \mathbf{q}^i) d\ell = 0 \quad (2)$$

where \mathbf{q}^i and \mathbf{q}^e are the inertial and external (hydrodynamic, gravitational and buoyancy) per unit length forces acting on the element, σ and $\delta\varepsilon$ are the axial stress and the incremental variation of the axial strain caused by the relative motion of the element ends P and Q, and V_0 the volume of the undeformed element.

Using Green's definition of the axial strain [Crisfield, 1991],

$$\varepsilon = \frac{dr_n^2 - dr_0^2}{2dr_0^2} \quad (3)$$

the variation $\delta\varepsilon$ is determined.

We define the differentials dr_0 and dr_n along the initial P_0Q_0 and deformed element P_nQ_n respectively as,

$$dr_0 = \frac{d\mathbf{r}_0}{d\xi} d\xi, \quad dr_n = \frac{d\mathbf{r}_n}{d\xi} d\xi = \frac{d(\mathbf{r}_0 + \mathbf{u})}{d\xi} d\xi \quad (4)$$

Assuming a linear variation of geometry and displacements along the length of the element, it holds:

$$dr_0^2 = d\mathbf{r}_0^T \cdot d\mathbf{r}_0 = \frac{d\mathbf{r}_0^T}{d\xi} \frac{d\mathbf{r}_0}{d\xi} d\xi d\xi = \alpha_0^2 d\xi d\xi \quad (5)$$

$$dr_n^2 = d\mathbf{r}_n^T \cdot d\mathbf{r}_n = \left(\frac{d\mathbf{r}_0^T}{d\xi} \frac{d\mathbf{r}_0}{d\xi} + 2 \frac{d\mathbf{r}_0^T}{d\xi} \frac{d\mathbf{u}}{d\xi} + \frac{d\mathbf{u}^T}{d\xi} \frac{d\mathbf{u}}{d\xi} \right) d\xi d\xi$$

Substitution of (5) into (3) gives the strain displacement relation:

$$\varepsilon = \frac{dr_n^2 - dr_0^2}{2dr_0^2} = \frac{1}{\alpha_0^2} \frac{dr_0^T}{d\xi} \frac{d\mathbf{u}}{d\xi} + \frac{1}{2\alpha_0^2} \frac{d\mathbf{u}^T}{d\xi} \frac{d\mathbf{u}}{d\xi} \quad (6)$$

Considering that the displacements of the two end nodes P and Q of the element are degrees of freedom (d.o.f) of the problem, the displacement of any intermediate point along the element is written as

$$\mathbf{u} = \mathbf{N} \cdot \mathbf{p} \quad , \quad \mathbf{p}^T = \left\{ \underbrace{u_1 \quad v_1 \quad w_1}_{\text{node P}} \quad \underbrace{u_2 \quad v_2 \quad w_2}_{\text{node Q}} \right\} \quad (7)$$

where,

$$\mathbf{N} = \begin{bmatrix} 1/2 \cdot (1-\xi) & 0 & 0 & 1/2 \cdot (1+\xi) & 0 & 0 \\ 0 & 1/2 \cdot (1-\xi) & 0 & 0 & 1/2 \cdot (1+\xi) & 0 \\ 0 & 0 & 1/2 \cdot (1-\xi) & 0 & 0 & 1/2 \cdot (1+\xi) \end{bmatrix} \quad (8)$$

is the matrix of the shape functions considered linear in the present analysis. In a similar manner (using the same linear interpolation functions) the coordinates of the arbitrary point R_0 along the undeformed element can be defined if the coordinates of the end points $P_0 (x_1, y_1, z_1)$ and $Q_0 (x_2, y_2, z_2)$ are known,

$$\mathbf{r}_0 = \mathbf{N}\mathbf{x} \quad , \quad \mathbf{x}^T = \{x_1 \quad y_1 \quad z_1 \quad x_2 \quad y_2 \quad z_2\} \quad (9)$$

Using (7) and (9) and (6) the incremental variation of the strain $\delta\varepsilon$ can be expressed in terms of the virtual displacement $\delta\mathbf{p}$ of the element end nodes:

$$\delta\varepsilon = \left(\frac{1}{\alpha_0^2} \frac{dr_0^T}{d\xi} \mathbf{N}_\xi \right) \delta\mathbf{p} + \left(\frac{1}{\alpha_0^2} \frac{d\mathbf{u}^T}{d\xi} \mathbf{N}_\xi \right) \delta\mathbf{p} = \left(\frac{1}{\alpha_0^2} (\mathbf{x} + \mathbf{p})^T \mathbf{N}_\xi^T \mathbf{N}_\xi \right) \delta\mathbf{p} = \mathbf{b}^T \cdot \delta\mathbf{p} \quad (10)$$

where in the above expression the matrix $\mathbf{N}_\xi = d\mathbf{N} / d\xi$ is constant along the length of the element, due to the linear shape functions considered.

The stress field is determined through application of Hooke's laws by making the assumption of linear elastic material:

$$\sigma = E \varepsilon \quad (11)$$

As already stated, the Young modulus E of the twine material will be different in compression and extension. The compression value will be equal to zero but in practical terms is taken very small, for numerical stability.

By introducing (10) into (2) and integrating over the cross section area A_0 , the following system of non-linear dynamic equations is obtained:

$$\int_{-1}^1 \mathbf{N}^T (\mathbf{q}^e - \mathbf{q}^i) \alpha_0 d\xi = \int_{-1}^1 \mathbf{b} \sigma A_0 \alpha_0 d\xi = 2\alpha_0 A_0 \mathbf{b} \sigma = \mathbf{f} \quad (12)$$

From the above derivation, it is made clear that the non linearity of equations (12) lies in two distinct reasons. The first is the inherent capability of the model to accommodate both large displacements and deformations (geometric non-linearity) through the use of Green's strain definition in its non linear form. The second is due to the different stiffness characteristics of the elements in tension and compression (material non-linearity). However, non linearity of the stress-strain state equations is not addressed in the present work (as done by Tsukrov et al 2005).

Non linear equations (12) are next expressed in perturbed form (linearization about a reference deflected position \mathbf{p}^0) and then solved iteratively, until perturbations converge to zero. Taylor's expansion of the non linear expression of the internal loads \mathbf{f} about a reference deflected position \mathbf{p}^0 yields:

$$\mathbf{f} = \mathbf{f}(\mathbf{x} + \mathbf{p}^0) + \frac{\partial \mathbf{f}}{\partial \mathbf{p}} \cdot \Delta \mathbf{p} = \mathbf{f}(\mathbf{x} + \mathbf{p}^0) + \mathbf{K}_t \cdot \Delta \mathbf{p} \quad (13)$$

Thereby, the element tangent stiffness matrix \mathbf{K}_t is obtained. If the density of the material of the twine ρ is assumed constant along its length then:

$$\begin{aligned} \int_{-1}^1 \mathbf{N}^T \mathbf{q}^i \alpha_0 d\xi &= \int_{-1}^1 \mathbf{N}^T (\rho A_0)_w \ddot{\mathbf{r}}_n \alpha_0 d\xi = \int_{-1}^1 \mathbf{N}^T (\rho A_0)_w \ddot{\mathbf{u}} \alpha_0 d\xi = \\ &= \underbrace{\left[\int_{-1}^1 (\mathbf{N}^T (\rho A_0)_w \mathbf{N}) \alpha_0 d\xi \right]}_{\mathbf{M}} \ddot{\mathbf{p}} = \mathbf{M} \cdot \ddot{\mathbf{p}} \end{aligned} \quad (14)$$

where, $(\rho A_0)_w$ is the linear mass distribution of the wet twine (original dry mass increased by the water trapped within the twine fibers). The external loads, comprising the hydrodynamic and hydrostatic (buoyancy) forces on the element as well as the gravity loads are denoted with \mathbf{Q} :

$$\mathbf{Q} = \int_{-1}^1 \mathbf{N}^T \mathbf{q}^e \alpha_0 d\xi \quad (15)$$

They are non-linear, since they depend on the velocity in a nonlinear (quadratic) manner. Their linearization is treated in the next section. Combining (12), (13), (14) and (15) the final linearized system of the dynamic equations of the truss element takes the form:

$$\mathbf{M} \cdot \Delta \ddot{\mathbf{p}} + \mathbf{K}_t \cdot \Delta \mathbf{p} = \mathbf{Q} - \mathbf{M} \cdot \ddot{\mathbf{p}}^0 - \mathbf{f}(\mathbf{x} + \mathbf{p}^0) \quad (16)$$

The above set of equations represents the dynamic equations of a single element. For multi-element configurations like the fishing net, the local matrices of the various elements are assembled to global matrices for the full configuration in the standard FEM way. In this assembling procedure no coordinates transformation is needed because the dynamic equations (14) of the single element have been expressed in the global inertial frame.

The final set of equations is integrated in time using the Newmark second order implicit scheme [Bathe, 1996]. In every time step of the simulation the equations are solved iteratively until $\Delta \mathbf{p}$ goes to zero, by applying a full Newton-Raphson iterative scheme.

2.2 External loads

The external loads \mathbf{q}^e on the fishing net consist of (a) the hydrodynamic forces due to the relative motion (velocity and acceleration) of the net and the surrounding fluid, (b) the effect of buoyancy, and (c) the gravity loads. Amongst them, only the hydrodynamic forces are non-linearly coupled to the d.o.f's \mathbf{p} of motion of the net elements. Buoyancy and gravity forces are constant and only depend on the geometric and material properties of the elements. The hydrodynamic loads establish a non-linear hydro-elastic interaction. Thereby, hydrodynamic forces appearing in (16) must be linearized about the reference state \mathbf{p}^0 similar to internal and inertial loads.

For the calculation of the hydrodynamic forces on the elements of the net, Morison's (1950) equation is applied. It is appropriately modified to account for the relative motion of the twines with respect to the sea water [see Tsukrov et al, 2003]. According to Haritos and He (1992), the force per unit length on the twines (considered cylindrical) is given by:

$$\mathbf{q}_{hydro}^e = \mathbf{C}_1 \cdot \mathbf{V}_{Rn} + \mathbf{C}_2 \cdot \mathbf{V}_{Rt} + \mathbf{C}_3 \cdot \dot{\mathbf{V}}_{\infty n} + \mathbf{C}_4 \cdot \dot{\mathbf{V}}_{Rn} \quad (17)$$

where \mathbf{V}_{Rn} and \mathbf{V}_{Rt} are the normal and tangential to the element components of the relative velocity of the water, $\dot{\mathbf{V}}_{\infty n}$ is the normal to the element component of the water acceleration and $\dot{\mathbf{V}}_{Rn}$ is the normal to the element component of the water relative acceleration (see Figure 4) given by:

$$\begin{aligned}\mathbf{V}_{Rn} &= ((\mathbf{V}_{\infty} - \dot{\mathbf{u}}) \cdot \mathbf{n}_v) \mathbf{n}_v = ((\mathbf{V}_{\infty} - \mathbf{N}\dot{\mathbf{p}}) \cdot \mathbf{n}_v) \mathbf{n}_v \\ \mathbf{V}_{Rt} &= ((\mathbf{V}_{\infty} - \dot{\mathbf{u}}) \cdot \mathbf{t}) \mathbf{t} = ((\mathbf{V}_{\infty} - \mathbf{N}\dot{\mathbf{p}}) \cdot \mathbf{t}) \mathbf{t} \\ \dot{\mathbf{V}}_{Rn} &= ((\dot{\mathbf{V}}_{\infty} - \dot{\mathbf{u}}) \cdot \mathbf{n}_a) \mathbf{n}_a = ((\dot{\mathbf{V}}_{\infty} - \mathbf{N}\ddot{\mathbf{p}}) \cdot \mathbf{n}_a) \mathbf{n}_a \\ \dot{\mathbf{V}}_{\infty n} &= ((\dot{\mathbf{V}}_{\infty}) \cdot \mathbf{n}_a) \mathbf{n}_a\end{aligned}\tag{18}$$

In the above expressions, \mathbf{t} is the unit vector along the element length and \mathbf{n} is the unit vector normal to the element, on the plane defined by the relative velocity (or acceleration) and vector \mathbf{t} .

The coefficients of equation (17) are given by the following expressions:

$$C_1 = \frac{\rho_w}{2} C_n d V_{Rn}, \quad C_2 = C_t, \quad C_3 = \rho_w \cdot A \quad C_4 = \rho_w \cdot A \cdot C_m\tag{19}$$

Where d and A , are the diameter and the cross section area of the element respectively, ρ_w is the water density, C_n and C_t are the normal and tangential to the element drag force coefficients and C_m the added mass coefficient. The above expression gives good predictions of the hydrodynamic force on cylindrical elements the diameter of which is small compared to the wave lengths involved in the computation [Morison, 1950].

The normal and tangential force coefficients are given as functions of the Reynolds number

Re_n [Tsukrov et al, 2003]:

$$C_n = \begin{cases} \frac{8\pi}{(Re_n s)} (1 - 0.87 \cdot s^{-2}) & (0 < Re_n \leq 1) \\ 1.45 + 8.55 \cdot Re_n^{-0.90} & (1 < Re_n \leq 30) \\ 1.10 + 4.00 \cdot Re_n^{-0.50} & (30 < Re_n \leq 10^5) \end{cases}\tag{20}$$

and

$$C_t = \pi\mu (0.55 \cdot \text{Re}_n^{1/2} + 0.084 \cdot \text{Re}_n^{2/3}) \quad (21)$$

where

$$s = -0.077215665 + \ln(8/\text{Re}_n) \quad (22)$$

and

$$\text{Re}_n = \frac{\rho_w d V_{Rn}}{\mu} \quad (23)$$

where μ is the water dynamic viscosity. The added mass coefficient C_m , usually takes the value

$$C_m = 0.5.$$

Hydrodynamic drag force also acts on the leading weights dragging the net towards the sea floor. In the present dynamic analysis, the leading weights are considered as concentrated masses of spherical shape centered at the nodes of the truss elements. In this case, their drag force is given by:

$$\mathbf{q}_{hydro\ weights}^e = C'_1 \cdot \mathbf{V}_R + C'_3 \cdot \dot{\mathbf{V}} + C'_4 \cdot \dot{\mathbf{V}}_R \quad (24)$$

where again subscript R denotes relative velocity/acceleration, and:

$$C'_1 = \frac{\rho_w}{2} A_s C_{Ds} V_R, \quad C'_3 = \rho_w V_s \quad \text{and} \quad C'_4 = \rho_w V_s C_m \quad (25)$$

where A_s and V_s , are the projected to the flow area and the volume of the sphere of diameter D_s .

Finally gravitational loads, as well as buoyancy are taken into account on the net elements as well as on the leading weights. On the truss elements, the force per unit length is given by:

$$\mathbf{q}_{grav/buoy}^e = (\rho_w - \rho) \cdot \mathbf{g} \cdot \frac{\pi d^2}{4} \quad (26)$$

where \mathbf{g} is the gravitational acceleration vector. Similarly the concentrated gravity force on the weights is:

$$\mathbf{q}_{grav/buoy\ weights}^e = (\rho_w - \rho) \cdot \mathbf{g} \cdot V_s \quad (27)$$

Summing up all the above contributions, the external loads matrix \mathbf{Q} is written as:

$$\begin{aligned}
\mathbf{Q} = & \int_{-1}^1 \mathbf{N}^T \mathbf{q}_{hydro}^e \alpha_0 d\xi + \int_{-1}^1 \mathbf{N}^T \mathbf{q}_{grav/buoy}^e \alpha_0 d\xi + \\
& + \sum_k \int_{-1}^1 \mathbf{N}^T \mathbf{q}_{hydro\ weights}^e \delta(\xi - \xi_k) \alpha_0 d\xi + \sum_k \int_{-1}^1 \mathbf{N}^T \mathbf{q}_{grav/buoy\ weights}^e \delta(\xi - \xi_k) \alpha_0 d\xi
\end{aligned} \tag{28}$$

where, δ denotes the Dirac function. The use of Dirac function implies that concentrated forces are applied at certain positions ξ_k along the elements. The summation is taken over the number of weights distributed over the twine. Taking into account that the leading weights are usually placed at the nodes of the element, the maximum number of weights per element is two.

An approximate linearization of the hydrodynamic loads about the current configuration (i.e. without taking into account the variations of the established unit vectors $\mathbf{n}_v, \mathbf{t}, \mathbf{n}_a$ \mathbf{v} and \mathbf{a}) results in the following additional mass and damping matrices:

$$\begin{aligned}
\mathbf{C}_{hydro} = & \int_{-1}^1 \mathbf{N}^T C_1 \mathbf{n}_v \mathbf{n}_v^T \mathbf{N} \alpha_0 d\xi + \int_{-1}^1 \mathbf{N}^T C_2 \mathbf{t} \mathbf{t}^T \mathbf{N} \alpha_0 d\xi \\
& + \sum_k \int_{-1}^1 \mathbf{N}^T C'_1 \mathbf{v} \mathbf{v}^T \delta(\xi - \xi_k) \mathbf{N} \alpha_0 d\xi
\end{aligned} \tag{29}$$

$$\mathbf{M}_{hydro} = \int_{-1}^1 \mathbf{N}^T C_4 \mathbf{n}_a \mathbf{n}_a^T \mathbf{N} \alpha_0 d\xi + \sum_k \int_{-1}^1 \mathbf{N}^T C'_4 \mathbf{a} \mathbf{a}^T \delta(\xi - \xi_k) \mathbf{N} \alpha_0 d\xi \tag{30}$$

where $\mathbf{v} = \mathbf{V}_R / |\mathbf{V}_R|$ and $\mathbf{a} = \dot{\mathbf{V}}_R / |\dot{\mathbf{V}}_R|$.

Besides the external forces acting on the weights, their inertia loads must be also taken into account.

This is done by adding the following additional mass matrix to the original mass matrix of (14):

$$\mathbf{M}_{weights} = \sum_k \int_{-1}^1 \mathbf{N}^T m_{weight} \delta(\xi - \xi_k) \mathbf{N} \alpha_0 d\xi \tag{31}$$

Based on the above derivation system (16) takes the form:

$$(\mathbf{M} + \mathbf{M}_{weights} + \mathbf{M}_{hydro}) \cdot \Delta \ddot{\mathbf{p}} + \mathbf{C}_{hydro} \cdot \Delta \dot{\mathbf{p}} + \mathbf{K}_t \cdot \Delta \mathbf{p} = \mathbf{Q}^0 - (\mathbf{M} + \mathbf{M}_{weights}) \cdot \ddot{\mathbf{p}}^0 - \mathbf{f}(\mathbf{x} + \mathbf{p}^0) \tag{32}$$

2.3 Definition of the equivalent net

Given the extremely high number of cells in a real fishing net, it becomes impractical to simulate the real net, because in this case the memory and computational time requirements would be vast. As an example for a purse seine with dimensions 800x120 m - typical dimensions for deep water fishing in the Aegean sea – the number of cells would be $64000 \times 14000 = 8.96 \cdot 10^8$. For this reason it is convenient to define a consistent equivalent net with a bigger size than that of the real net (several cells of the real net can fit into one cell of the equivalent net) which however exhibits a similar hydroelastic behavior. The new equivalent net is defined in such a way that there is similarity of the hydrodynamic drag is satisfied [Tsukrov et al, 2003]. The way that the equivalent net is defined depends a lot on the shape of the cell (whether they are of square or of diamond type). In either case, the total strand length of the net needs to be determined which for a net with square type cells is:

$$L_{\text{total}} = (n_2 \cdot (2n_1 + 1) + n_1) \cdot \ell \quad (33)$$

where ℓ is the half mesh size, as shown in Figure 6 and n_1, n_2 is the number of cells in each direction: lengthwise and depth respectively, shown in Figure 5. Accordingly, in the case of a net with diamond shape cells the total strand length is given by:

$$L_{\text{total}} = 4n_1 n_2 \ell \quad (34)$$

The calculation of the diameter D_{eq} of the equivalent net twines is performed in such a way that the total projected area to the flow remains the same. To this end, if n_1, n_2 is the number of cells in each direction of the real net and L_{total} is the total strand length of the net and $n_{\text{eq}1}, n_{\text{eq}2}$ and $L_{\text{eq total}}$ denote the same parameters for the equivalent net, by considering that:

$$n_2 / n_{\text{eq}2} = n_1 / n_{\text{eq}1} = \ell_{\text{eq}} / \ell = a \quad a > 1 \quad (35)$$

where ℓ_{eq} is the half mesh size of the equivalent net, the equivalent diameter is given by

$$D_{\text{eq}} \cdot L_{\text{eq total}} = d \cdot L_{\text{total}} \quad (36)$$

The equivalent D_{eq} diameter is used in the calculation of the hydrodynamic forces as presented in the previous section, while the real diameter d is used in determining the Reynolds number of the flow Re_n . As argued by Tsukrov et al (2003), through the above definition of the equivalent diameter the

mass of the net is not retained. In order to retain the total mass, the cross section area of the equivalent net strands is not calculated on the basis of D_{eq} . Instead the following expression is used:

$$A_{eq} = \frac{\pi \cdot d^2}{4} \cdot \left(\frac{D_{eq}}{d} \right) = \frac{\pi \cdot d^2}{4} \cdot \left(\frac{L_{total}}{L_{eq\ total}} \right) \quad (37)$$

The equivalent cross section area A_{eq} is used in calculating the linear mass distribution of the equivalent twine $(\rho A)_{eq}$ as well as its axial stiffness $(EA)_{eq}$ considering that the material density ρ and Young's modulus E are that of the actual twine.

3. Model Validation

3.1 Hydrodynamic model validation against semi-empirical formulas

In the present section, the hydrodynamic model presented in section 2.2 and 2.3, (including the equivalent net definition) is validated against various semi-empirical formulae proposed in the literature. Semi empirical formulae found in the literature have been derived by means of appropriate fitting to measurements on net panels, usually of square type mesh. The present validation is extended in a following section with comparisons against measurements performed at NTUA's towing tank on a typical purse seine with diamond type mesh.

It is common that drag force F_D of a net panel is expressed as function of a non-dimensional drag coefficient. For a net panel having outline dimensions $a \times b$ and positioned normal to the free stream, Kawakami's (1959 and 1964) definition of the drag coefficient is given by:

$$F_D = \frac{\rho_w}{2} C_d V^2 L d \quad (38)$$

where C_d is the mesh drag coefficient, ρ_w the water density, V the free stream velocity, d the twine diameter; and L the total length of twine, which may be approximated by:

$$L \cong 2 \frac{ab}{\ell} = 2 \frac{A_{out}}{\ell} \quad (39)$$

(or calculated by (33) or (34) depending on the cell type) where ℓ is the half mesh size of the net (i.e. the length between adjacent knots); and $A_{\text{out}} = a \cdot b$ the outline area. The projected area Ld used in equation (38), becomes then:

$$Ld = A_{\text{out}} \frac{2d}{\ell} \quad (40)$$

where $S = 2d/\ell$ is the solidity ratio of the net. The above definition of solidity, as obtained through equation (40) is not universal. As discussed in Tsukrov et al (2011) it depends on the type of the mesh, whether it formed by rectangular or diamond shape cells but also on the 3D nature of the intertwines.

Based on Kawakami definition, Milne (1972) proposed the following empirical formula for the drag coefficient of a knotless net, positioned normal to the free stream velocity:

$$C_d = 1 + 2.73 \frac{d}{\ell} + 3.12 \left(\frac{d}{\ell} \right)^2 \quad (41)$$

Aarsnes et al (1990) derived expressions of the lift and drag force on an inclined, with respect to the free stream velocity direction, net panel based on experimental observations. The drag coefficient C_D and lift coefficient C_L in Aarsnes formulae is referred to the outline area S of the net. According to this definition the total force on the net will be written as:

$$\mathbf{F} = \mathbf{D} + \mathbf{L} = \frac{\rho_w}{2} C_D S \mathbf{V} \mathbf{V} + \frac{\rho_w}{2} C_L S \mathbf{V}^2 \mathbf{n}_L \quad (42)$$

and the lift and the drag coefficients are given by:

$$C_D = 0.04 + \left[-0.04 + 2.00 \frac{d}{\ell} - 4.96 \left(\frac{d}{\ell} \right)^2 + 109.60 \left(\frac{d}{\ell} \right)^3 \right] \cos \alpha_w \quad (43)$$

$$C_L = \left[1.14 \frac{d}{\ell} - 14.16 \left(\frac{d}{\ell} \right)^2 + 80.80 \left(\frac{d}{\ell} \right)^3 \right] \sin 2\alpha_w$$

where α_w is the angle formed between the free stream velocity \mathbf{V} and the vector \mathbf{n} normal to the net panel (directed downstream). The direction of the lift force is defined through the unit vector \mathbf{n}_L (normal to the free stream velocity) that can be expressed in terms of \mathbf{V} and \mathbf{n} by:

$$\mathbf{n}_L = \frac{(\mathbf{V} \times \mathbf{n}) \times \mathbf{V}}{|(\mathbf{V} \times \mathbf{n}) \times \mathbf{V}|} \quad (44)$$

As seen in (43), Aarsnes drag formula contains a constant term that accounts for the drag on the panel that is parallel to the current direction ($\alpha_w = 90^\circ$).

Formulae (41) and (43) were based on experiments with plane nets having solidity ratios in the range between 0.13 and 0.30. Furthermore, formula (43) was based on measurements with a Reynolds number (defined on the basis of the twine diameter) in the range from 1400 to 1800, as noted by Lader and Enerhaug (2005) and Lader and Fredheim (2006). The empirical formulation was optimized for the middle solidity ratio range. The formulae provide a constant value for the drag coefficient, independently of the Reynolds number.

Solidity being the most convenient geometrical parameter obviously does not cover all field of parameters defining the drag force on the net. Zhan et al (2006) conducted experiments in a towing tank on planar nets and examined the effects of Reynolds number, net solidity and flow direction on the drag force. The solidity ratios were in the range from 0.128 to 0.223 while Reynolds numbers ranged from 170 to 1400. Exploiting their experimental results, the following formula for the normal drag coefficient was proposed:

$$C_d = 1 + \frac{0.137}{V} + 1.002 \frac{d}{\ell} + 2.230 \left(\frac{d}{\ell} \right)^2 \quad (45)$$

A more recent formula of the drag on nets is that due to Balash et al (2009), who proposed an analytical model and a corrected formula based on experimental data. The analytical formula utilizes the drag coefficient of circular cylinders C_D^{cyl} from White (1974):

$$C_D^{cyl} = 1 + 10 \text{Re}_n^{-2/3} \quad \text{Re}_n \leq 5 \times 10^3 \quad (46)$$

and defines the drag coefficient on the basis of the outline area A_{out} as:

$$C_D = C_D^{cyl} \frac{S}{(1-S)^2} \quad (47)$$

The corrected formula was obtained through least square fitting to experimental data and is given by:

$$C_D = C_D^{cyl} (8.03S^2 - 0.74S + 0.12) \quad (48)$$

Balash argued that in order to calculate the drag force of inclined nets with respect to the incoming flow, one can apply the formula derived by Stekalova (1964):

$$C_D(\alpha_w) = C_D \sin^3\left(\frac{\pi}{2} - \alpha_w\right) \quad (49)$$

In the sequel predictions of the hydrodynamic loads on a net panel with square type mesh are presented and compared against the above discussed semi-empirical formulae. Loads on the net are calculated for different values of the free stream velocity and orientation of the net panel with respect to the free stream velocity.

The geometric and structural parameters of the benchmark net considered in the present analysis are [Tsukrov et al, 2003]: half mesh size $\ell = 0.0155$ m, twine diameter $d = 0.0016$ m, strand material density $\rho = 1150$ kg / m³ and Young modulus $E = 2 \times 10^9$ Pa. The range of the Reynolds number variation (as defined in (23), with reference to the twine diameter) considered in the analysis is $35 \div 1400$, for a free stream velocity range $0.025 \div 1$ m / s.

For the simulation of 1 m^2 panel, an equivalent net with mesh size 20×20 (equivalent mesh ratio $a = n / n_{eq} = 3.2$) is used, as shown in Figure 7. In the same figure, the deformed state of the net is presented for 1 m/s current velocity. Given that the net is set perpendicular to the free stream velocity and is supported along its perimeter the highest deformation appears at the centre.

In Figure 8 and Figure 9, the drag force per square meter of the net and the drag coefficient C_D are shown as function of the incoming current speed, for a net panel placed perpendicular to the free stream velocity ($\alpha_w = 0^0$). The agreement of the FEM code with Milne and Aarsnes predictions is better at high current speeds. This was expected since, as already discussed, the abovementioned formulae are calibrated at high Reynolds numbers. Balash's formula predicts 15% higher drag for current speeds higher than 0.2 m/s ($Re > 280$) This is in agreement with the results reported in Tsukrov et al (2011) where drag predictions on nets of different geometry and material are compared to measurements. On the other hand better agreement is obtained for very low Reynolds numbers. The shape of the C_D curve predicted by the FEM model is similar to that obtained using Zhan's and Balash's formulae, which both account for the variation of the drag with Reynolds number. Both curves increase rapidly at low current speeds, corresponding to Reynolds number below 400,

with Zhan's formula though providing significantly higher C_D values both compared to the FEM code but also to Balash's formula. It is noted that at high current speeds, the model predicts slightly lower drag as compared to all analytical expressions. Closer is the agreement with Zhan's formula.

Figure 10 and Figure 11 present drag and lift force per square meter of the same net panel as function of the inclination angle of the panel α_w . The current speed is taken equal to 0.5 m/s . It is noted that for moderate incidence angles, up to 40° , the shape of the variation compares well with Aarsnes results. There is a slight under-prediction of the drag consistent with the results presented earlier for the 0° case. For the same range, the lift coefficient shows a very good agreement. For inclination angles higher than $50^\circ - 60^\circ$ predictions of the present method start to deviate from Aarsnes results. It is seen that, as the incidence angle increases, the drag force tends asymptotically to a constant value while Aarsnes predictions indicate that the drag force continuously drops with increasing angle. The drag value obtained with the present model at 90° angle of the panel is considerably higher than that predicted by Aarsnes' formula. The reason for the above difference is that as the flow gets parallel to the net plane, flow shading effect from the upwind twines to the downstream ones become higher. As a result downstream twines experience lower speeds and therefore drag force on them is lower. This shading effect is not taken into account in the present model. Balash's formula in conjunction with (49) to account for the effect of the inclination of the net panel with respect to the free flow, predicts a much faster reduction of the drag which almost drops to zero beyond 75° inclination angle.

As concerns lift force, it is consistently under-predicted in the range of α_w angles that drag is over-predicted. However, the zero lift value at $\alpha_w = 90^\circ$ is captured by the model.

3.2 Hydro-elastic model validation

There are certain difficulties involved with the validation of the hydro-elastic model based on existing simulation or test results for fishing nets. First, most of the test and simulation results available in the literature concern specific fishing net designs the exact geometric or structural characteristics of which are not available [Shimizu et al, 2005]. Moreover, tests were conducted for complete fishing gears containing additional members such as sinkers, buoys, pursing wires. Such complicated systems involve a lot of uncertainty and they cannot serve the basic validation of the structural model. On the other hand several simple benchmark examples concerning cables and mooring lines can be found in

the literature. In the present paper baseline validation of the hydro-elastic model is performed for such a simple test example. In a following section, validation is extended to comparisons against in situ observations performed at NTUA's towing tank on a real fishing net with known structural and geometric characteristics.

The test case and experimental data on which validation of the present truss element model is based, is taken from Lo and Leonard (1982). It concerns relaxation of a single point mooring cable attached to a floater, immersed in still water environment as shown in Figure 12. The buoy is displaced from its neutral position and then is released to return back to it. This is a simple example to assess the model capabilities in predicting the hydrodynamic behavior of the cable which constitutes the first step in the consistent modeling of a fishing net, containing a large number of interconnected elements. In the present example the un-stretched length and the diameter of the cable are 1.82 m and 4.14 mm respectively, the weight of the cable in the air 0.167 N / m and in water 0.0347 N / m, the stiffness of the cable 21.4 N, the diameter of the floater 50.8 mm, the weight of the floater in the air 0.11 N and in the water -0.538 N. The added mass coefficient for the cable is taken $C_m = 1$ and for the buoy $C_m = 0.5$ while the water dynamic viscosity is taken $\mu = 1.13 \times 10^{-3}$ Ns / m². The added mass coefficient of the buoy was selected in accordance with the definitions of Haritos and He (1992) who have also simulated the same case.

In the simulations the cable was modeled by a number of 15 truss elements of equal length. The time step used was $\Delta t = 0.005$ s. Before simulating the transient response of the cable while moving from each disturbed position towards its equilibrium position, the deformed cable state at the displaced position needs to be defined first. At this stage the effect of the cable/sea bed interaction was taken into account. The reaction force of the sea floor was simulated through constant springs applied at the nodes of the truss elements. The stiffness of the springs becomes very high when the nodes approach the sea floor level. The deformed state of the cable at the displaced position was defined through a time domain simulation in which the cable/buoy attachment node was constrained and the cable was released from some initial arbitrary position to reach equilibrium.

Figure 13 and Figure 14 present the vertical and horizontal motion of the buoy in the first 3s after it has been released. Comparison against test results from Lo and Leonard (1992) shows good agreement with the test data for both d.o.fs of motion. A small difference is seen in the vertical

displacement after the first 0.5s which is also noted in the simulation results presented by Lo and Leonard (1992). The quicker return to equilibrium indicates lower hydrodynamic drag predicted by the model. This implies that the drag of the buoy might have been underestimated. Figure 15 shows the return velocity of the buoy. It is noted that the test data exhibit a very large scatter. However, predictions of the maximum speed at the beginning of the buoy's motion and also of the rate at which this speed drops in the sequel compare well with the test data. Finally, Figure 16 presents the tension at the bottom of the cable at the connection with the sea floor. It is seen that also in terms of loads consistent results are provided.

4. Test campaign results and comparison with FEM predictions

The hydrodynamic behavior of a purse seine net was investigated in the towing tank of the Laboratory for Ship and Marine Hydrodynamics, of the National Technical University of Athens (NTUA). The rectangular basin of the tank is 100m long, 5m wide and 3.5m deep. The tank is equipped with a carriage, capable to tow models at speeds up to 5 m/sec.

The aim of the test was: (a) to measure the drag on the net for different inclination angles α_w (b) to assess its submergence behaviour in terms of the critical submergence speed and deployment time. The properties of the examined purse seine including the dimensions of the leading weights and the weight of the upper and lower rope are shown in Table 1. This is a typical example of the kind of nets being used in the Mediterranean Sea. Test results are compared to predictions of the FEM tool described and validated in the previous sections. Cross checking of the FEM predictions and experimental observations is also carried out against the results of a simplified one dimensional submersion model.

4.1 Resistance tests – comparisons with FEM code

Aim of the measurements was to examine the net in conditions similar to that encountered during the submergence phase, i.e. without trawling forces. To this extent, a sample of the net was extracted from a larger purse seine, taking special care to avoid any stretching, which could result in a deviation in the net geometry. Thus, the seine was laid down and got the shape determined by tightening the upper and lower ropes. A section 2.315 m in height (about 230 cells) and 2.00 m in width (about

160 cells) was then extracted, attached to a rectangular aluminium frame and mounted on the load cell of the carriage, as shown schematically in Figure 17. In order to compensate for the frame resistance, the tests were conducted in two phases, the frame being outfitted with and without the net. The towing post of the carriage was instrumented with an R35-I Kempf & Remmers dynamometer, capable of measuring forces up to 200N, having a sensitivity of 1.8 mV/V at this load and an accuracy of 3.3%.

Figure 18-Figure 20 (a), show the measured drag (force in the direction of flow velocity), plotted against speed, for inclination angles $\alpha_w = 0^0$, 45^0 and 90^0 respectively. A quadratic best-fit curve is also included in the graphs and shown with a dashed line. The displayed values are valid for fresh water (temp. 22.4 °C) and correspond to the total drag force per unit of the outline area of the net. Also, Figure 18-Figure 20 (b) show a close up of the area of low speeds, up to 0.2 m/s. This range is of interest when studying the low speed submersion of the net.

In the same plots predictions of the FEM code are also presented. FEM simulations are performed for an equivalent net with mesh ratio $a = n / n_{eq} = 8$ (20×29 cells). The properties of the equivalent net have been defined following the analysis of section 2.3 and they are given in Table 2. An excellent agreement is obtained at $\alpha_w = 0^0$ both at low and high speeds. As the inclination angle increases deviations become higher. As a result of the shading effect, already discussed in section 3.1, higher drag is predicted at $\alpha_w = 45^0$ and 90^0 . At $\alpha_w = 45^0$ shading effect is small and therefore deviations are also expected to be small. However, at the inclination angle of 90^0 the predicted drag is more than double the measured one for all speeds.

Figure 21 presents the variation of the drag coefficient C_D , as function of the flow speed for all three inclination angles $\alpha_w = 0^0$, 45^0 and 90^0 . It is noted that due to the very small diameter of the net twines (0.35 mm) the Reynolds number range of the test was considerably lower than that of the benchmark case examined in section 3.1. For the current speeds varying in the range $0.05 \div 0.7$ m/s Reynolds varies in the range $15 \div 215$. Similar to the drag force the predicted drag coefficient agrees well with the measured data for the angle of 0^0 . Only at very low Reynolds numbers (current speed < 0.1 m/s) predictions slightly underestimate measured C_D , however, they reproduce the steep increase of C_D with decreasing flow speed. At 45^0 inclination angle predictions overestimate C_D at

high speeds while the opposite occurs at low speeds. Nevertheless, up to the angle of 45^0 predictions are still reasonably close to measurements. Finally big deviations are noted at 90^0 inclination where the predicted drag coefficient appears to be more than two times the measured one. The difference is higher at high current speeds.

In Figure 22, predicted and measured C_D for the inclination angle of 0^0 are compared to the results provided by the formulas of Aarsnes and Balash. For the diamond shape cells of the net, the solidity was defined according to the definition of Tsukrov et al (2011):

$$S = 2 \left(\sqrt{\left(\frac{n_1}{a}\right)^2 + \left(\frac{n_2}{b}\right)^2} \right) d \quad (50)$$

A better agreement with the results of Balash formula is obtained in terms of the shape of the variation of the drag coefficient with the current speed. Balash's formula overestimates drag coefficient by 15% as compared to the measured data. As discussed in the previous section this is expected since Balash formula accounts for the dependency of the drag coefficient with Reynolds number. On the other hand Aarsnes' formula considerably underestimates drag coefficient especially at very low Reynolds numbers. At higher Reynolds numbers, where it is supposed to perform better, the under-prediction is about 25%.

In Figure 23 the ratio of the measured over the predicted drag is shown as function of the free stream velocity. The ratio is calculated using the quadratic best fit curves shown in Figure 18-Figure 20 (dashed lines). It is noted that this ratio is almost independent of the flow speed for flow velocities beyond 0.2 m/s . At lower speeds the ratio rapidly increases but this is only because regression curves deviate from the measured data in the low speeds region. They provide higher drag values especially at $\alpha_w = 0^0, 45^0$ (see Figure 18(b) and Figure 19(b)) which reflects on the ratios shown in Figure 23. Based on the fact that the ratio of the measured to predicted drag is almost independent of the current velocity, a correction to the drag can be proposed in order to account of the drag reduction resulting from the twines shading effect. Such a correction factor is absolutely necessary in order to obtain consistent drag predictions of the submerging net. In such a case, the relative velocity (net diving velocity) is parallel to the net provided that the sea current and wave induced velocities are negligible (still water assumption). The correction curve shown in Figure 24, is tuned based on the measured to predicted drag ratios. It is noted that if the relative flow is parallel to the net (maximum

shading effect) the correction factor of the drag takes the value of 0.39. As will be shown in the next section, in the absence of a consistent flow shading model, the application of a global correction factor to the drag is considered absolutely necessary in the case of submerging nets, in order to obtain reasonable net deployment times.

In Figure 25, the drag coefficient of the net is presented as function of the inclination angle α_w . Results of the FEM, obtained using the above correction curve are compared to measurements (at the three measured angles $\alpha_w = 0^\circ$, 45° and 90°). The correction is applied on the basis of the local relative velocity associated with each cell of the net. After calculating this velocity, the correction is applied to each individual twine composing the cell. Moreover, results of Aarsnes and Balash formulae are plotted in the same figure. It is seen that Aarsnes results underestimate the drag coefficient at low inclination angles however they fit better at higher angles close to 90° . It is noted that Aarsnes' results are restrained by the fact that the dependency to Reynolds number is not taken into account.

Furthermore, at 90° inclination angle, the drag coefficient obtains a constant value of 0.04 independent of the solidity of the net or any other geometric parameter. In general, the cosine shape of the curve matches well the shape of the corrected for the shading effect predictions. As regards equation (49) which considers a cubic sinus dependency of the drag coefficient with the inclination angle, seems to predict an unrealistic drop of the drag coefficient with α_w as compared to the measured data. Moreover, the drag coefficient tends to zero at 90° which is not supported by the measurements.

Besides steady state tests and results, the dynamic behavior of the net is investigated under a current field combined with an airy wave. The wave period is $T=2$ s and the deterministic wave height is $H=0.5$. The analysis was performed for the test net immersed at the depth of 1 m in a water tank with a depth of 5 m. The current field is considered linearly varying from 0 m/s at the tank floor to 0.5 m/s at the mean water level. In Figure 26, the time history of the drag force and the displacement of the net midpoint are plotted for three values of the equivalent mesh rate, $a = n / n_{eq} = 4, 8, 16$. Aim of the analysis is to prove the consistency of the equivalent net in terms of the hydrodynamic loads but also its inertia characteristics. It is seen that grid independent solution is obtained even for coarser grids. Some small difference seen in the displacement of the midpoint of the net, appearing in the form of a small level shift, is due to the fact that the grid points of the various equivalent nets do not coincide and therefore the closest points are selected.

4.2 Submergence test – comparisons with FEM code and simplified model

The submergence tests were conducted on a large portion of the purse seine (approx. 20m in length), which was deployed on the water surface of the tank and left free to reach the bottom. The aim of these tests was to investigate the diving speed during the initial phase of submergence. To this end, the seine was released at the water level and subsequently left to fall freely, in front of vertical rulers. During the test, an underwater camera was used to record the downward motion (see Figure 27). The system made use of the Sony XC-7500 camera and the Matrox Meteor II frame grabber, capturing an area of 60x45 cm with a resolution of 640x480 pixels at a rate of 60 frames/sec.

Table 3 shows the measured submersion speeds, depths and time intervals from the beginning of the motion, based on the processing of the video recordings.

In order to capture and quantify the basic mechanics associated with the net submersion a simplified theoretical model for the motion of the net was developed. The model uses as input the drag data derived from the experimental work. It has been used as a basis for validating the experimental observations as well as the FEM code predictions.

The net was modeled as a one-dimensional, chain-like body, with infinite stiffness in tension and zero stiffness in compression moving in the vertical direction. This configuration is expected to lead to maximum submersion speed, since transverse forces, coming either from the net trawling or from sea currents, may significantly retard the submersion.

The seine is assumed to be initially folded and placed on the water surface (see Figure 28). At the beginning of the motion the net starts to deploy, with the lower heavy end submerging into the water and drawing down a progressively increasing portion of the seine. The equation of the dynamic equilibrium is derived through the application of the impulse-momentum principle. The instantaneous momentum of the whole system takes the form:

$$Q(t) = M\dot{z} + mz\dot{z} \quad (51)$$

where M is the mass (per width) of the lower rope and weights, including hydrodynamic added mass, m is the mass (per square meter) of the net and z the downwards displacement of the net.

Applying the impulse-momentum principle we get:

$$\Delta Q = \{W + w z - D(\dot{z}) - f(\dot{z})z\} \Delta t \quad (52)$$

where W , w are the submerged weight (gravity minus buoyancy) of the lower cable and the net respectively, D is the drag force (per unit length) of the lower cable (including the weight of the leading weights) and f is the drag force (per square meter) on the net.

Equations (51) and (52) give the following equilibrium equation:

$$M\ddot{z} + m\dot{z}^2 + mz\ddot{z} = W + w z - D(\dot{z}) - f(\dot{z})z \quad (53)$$

with initial conditions:

$$z(0) = \dot{z}(0) = 0 \quad (54)$$

The above equations are supplemented by the requirement of positive tension along the net, ensuring in this way the chain-like behavior and the one-dimensional character of the simplified model. In the opposite case, the net would buckle at a certain moment, under the action of a negative tension.

Tension varies linearly along the net:

$$T(\xi) = W - D(\dot{z}) + w(z - \xi) - f(\dot{z})(z - \xi) - M\ddot{z} - m\dot{z}^2 - m(z - \xi)\ddot{z} \quad 0 \leq \xi \leq z \quad (55)$$

The two extreme values are:

$$T(0) = m\dot{z}^2 \geq 0 \quad \text{and}$$

$$T(z) = W - D(\dot{z}) - M\ddot{z}$$

Thus, the condition of positive tension is fulfilled, provided that:

$$W - D(\dot{z}) - M\ddot{z} \geq 0 \quad (56)$$

Equations (53) and (56) are integrated numerically. Inertia and weight properties per unit length of the net and the lower rope carrying the leading weights are derived from the data provided in Table 1 and they are reported in Table 4. The drag of the leading weights is calculated assuming spherical weights. Summing up the drag of the weights and the drag of the lower rope the following expression of the viscous drag per unit length of the rope (including the weights) is obtained:

$$D = 4.152 \dot{z}^2 \quad (57)$$

The drag of the net is taken from the regression analysis on the measured data shown in Figure 20 that led to the following expression for $\alpha_w = 90^\circ$:

$$f = 11.066 \dot{z}^2 + 0.7256 \dot{z} \quad (58)$$

FEM simulations have been performed for an equivalent net with mesh ratio $a = n / n_{eq} = 32$. The properties of the equivalent net are given in Table 2. As already discussed in section 2.2 the weights are modeled as point masses of spherical shape which are placed at the nodes of the grid. The spacing of the grid points in the equivalent mesh is bigger (0.4 m) than the actual spacing of the weights (0.3 m). Thus, simulations are performed with a smaller number of bigger weights (in terms of mass and dimensions) while the total drag force on the weights is retained. This requirement is satisfied through the condition:

$$\frac{D_{eq}}{d} = \sqrt{\frac{n}{n_{eq}}} \quad (59)$$

where n , n_{eq} is the actual and equivalent number of weights and d , D_{eq} are the actual and equivalent diameter of the weights respectively.

In Figure 29, FEM predictions of the equivalent net geometry during the initial phase of the submergence are shown (time instants $t = 2, 4, 6$ and 10 s). The upper nodes of the mesh are constrained. Before the net is released it is folded close to the water surface (zero level in the figure). When the net is released it progressively deploys under the action of the weights. A contraction of the net is noted as a result of the sideways tension developing at the two ends. In the middle part of the net symmetry conditions lead to zero sideways tension and so the cells appear unstretched. This is an indication that the dynamic behavior of this portion of the net complies with the assumptions of the simplified one dimensional model. It also becomes clear that the net length to depth ratio is a critical parameter in order to ensure such a one dimensional behavior of the middle portion of the net.

In Figure 30 the time history of the submersion depth is shown. A good agreement of the predictions of both models with the observations is obtained, especially in the initial part of the submersion (at 4 s). Also the two models give very similar results, thus confirming the validity of the assumptions of the simplified model for the centre of the net. In Figure 31 predictions of the diving speed are compared to observations. In this figure three areas of interest are distinguished. The first corresponds

to the beginning of the event; the speed increases rapidly and reaches a maximum value, mainly due to the action of the lead weights. After this phase, the drag forces and the increasing inertia of the deploying system dominate and balance the action of the gravity. The speed is decreasing and eventually, during the last phase, reaches smoothly an asymptotic value. It is noted that the critical speed is captured well by the models (asymptotic value of the speed at third phase; an asymptotic formula for this parameter has been obtained by Katsaounis et al, 2009). For the second phase (net deceleration phase), measured velocity is unrealistically high (velocity at 4s) and does not seem to be in accordance with recorded depths and the agreement with predictions obtained therein. In this phase, a significant uncertainty was involved in the velocity measurements due to the fast change of the shape of the net, which at the beginning of the deployment has not yet acquired a planar form. In addition, the lower lead weights rope was not actually submerging as a straight line, mainly due to the influence of the weights and the flexibility of the net. As a result, the velocity at different points along the net was scattered and for this reason we are referring to 'observations' rather than 'measurements' of velocity.

In the FEM results presented in Figure 30 and Figure 31 a correction to the drag has been performed according to the correction factor shown in Figure 24 for $\alpha_w = 90^\circ$, in the absence of any current or wave induced velocity or relative motion due to trawling action. Thus, a correction factor 0.39 is applied according to Figure 24. In Figure 32 and Figure 33 FEM results for the depth and the speed are shown with and without the application of the correction factor. It is clear that under the action of a higher drag on the net both the initial phase and the critical velocity are significantly affected. Both the maximum speed reached at the initial drop phase as well as the critical diving speed, are quite lower. Also the deceleration rate in the second phase is quite bigger. Due to the higher drag, diving of the net is significantly retarded, which implies that a consistent modeling of the shading effect is absolutely necessary in order to obtain realistic values of the depths reached during submergence of the net. This is especially true in case that the aim of the simulation is to identify that the demand of the regulation that the net must not reach the sea floor during the trawling cycle is satisfied.

5. Net dynamic response in cyclic deployment

In the present section, the dynamic behavior of the purse seine in cyclic deployment is investigated. Cyclic deployment simulates the shooting phase of the fishing cycle where the auxiliary fishing boat

(skiff) releases the net while moving in a cyclic path. In the numerical simulations of the shooting phase we assume that the net is initially compacted at a very low depth (approximately 0.5 m below the sea level) and it is gradually deployed along the circumference of a cycle, the arc length of which is equal to the length of the lacing rope. We also assume that the nodes of the grid located on the lacing rope are constrained (zero displacements) along the cyclic path as shown in Figure 34. This assumption, made for the sake of simplicity, means that the lacing rope remains fixed in the cyclic path and cannot be drifted by sea currents. When the simulation starts, all the nodes of the grid are constrained. Cyclic motion of the boat and shooting of the net is simulated by gradually releasing nodes of the grid overtaken by the boat. We also assume that the fishing boat travels with a constant speed along the circumference of a cycle of constant radius.

In the simulations, an equivalent net, with a mesh ratio $a = n / n_{eq} = 256$ is used. This value of the mesh ratio is at least one order of magnitude higher than that employed in the preceding simulations. However, the use of finer meshes is prohibitive in terms of computational time and memory requirements. The dimensions of the purse seine modeled in the present study are 635 m x 65 m and consists of about 50000 cells in the circumferential direction and 7500 cells in the depth direction. This means that in order to simulate the real net one needs a computational grid consisting of about $7.5 \cdot 10^8$ cells and $2.25 \cdot 10^9$ d.o.fs. Even with a mesh ratio of $a = 256$ the equivalent net consists of about 10000 nodes ($3 \times 10000 = 30000$ d.o.fs) and the average computational time for the simulation of one fishing cycle is about 10 days on a cluster with 64 cores. For the modeling of the leading weights, the same approach to that of section 4.2 is followed. At the two edges of the fishing net two thin strips of stiffer net (bigger cells and thicker twines) are sutured. These strips prevent the net from acquiring its full length in the direction of depth and thereby reduce the maximum depth that the net reaches during submersion. The length of those strips is about 35 m, significantly lower than the length of the actual net (120 m) and almost equal to the maximum depth of the fishing site. For the modeling of those strips, equivalent stiffer cells are placed at the two edges of the net as shown in Figure 34. Two different speeds of the skiff are simulated, 1 m/s and 2 m/s respectively. In the simulations performed, sea currents are neglected. This corresponds to the most unfavorable situation in terms of the submersion depth, since in the presence of a component of the flow perpendicular to the plane of the net the drag force becomes higher. In Figure 35, two snapshots of the net submersion are shown. The first corresponds to the low speed and the boat has barely exceeded 270° azimuth while the second to the high and the boat has just completed the fishing cycle.

It is noted that the speed of 1 m/s is representative of skiffs used for fishing in the Aegean Sea. In Figure 36 and Figure 37 the submersion depths, of various points on the leading rope, corresponding to different azimuth locations along its circumference are shown for the two speeds respectively. It is seen that with the typical boat speed, the depth reached by the first quadrant of the net exceeds the limit of 30 m (dashed line in the plots), which corresponds to a representative depth of fishing sites in the Aegean Sea. For the particular depth, the sea bed will be reached long before the boat completes the fishing cycle. It is noted that although the first part of the net is constrained by the stiff strip attached to the edge, finally this part (located at 5° azimuth) will reach a depth of about 40 m. Furthermore, the part of the net which is located at 45° azimuth will go deeper at almost 45 m depth. As indicated by the vertical line of Figure 36, the net will touch the sea floor for the first time quite early, 260 s after the beginning of the fishing cycle when the boat is located at the azimuth of 135° . For the speed of 2 m/s (see Figure 37) the maximum depth reached by the net is about 25 m. In Figure 38 the submersion velocity is also presented for the same azimuth positions on the leading rope. It is seen that as in the case of the vertical submersion, the different points on the leading rope when released they obtain a high vertical velocity which is about equal to 0.5 m/s for all points. This is slightly lower than the maximum speed seen in the case of the vertical deployment. The difference is due to the loads acting to the moving net by the constrained (not yet released) part. For the same reason, the critical speed of the net is lower (about 0.05 m/s) and it is almost the same for all the positions along the leading rope. The transient of the submersion speed is very similar for the different points on the rope but for the first point at 5° azimuth which is constrained by the stiff strip at the edge of the net.

6. Conclusions

A general three dimensional hydro-elastic tool for the analysis of different types of fishing nets and aquaculture facilities was presented. The finite element formulation includes the concept of an equivalent net and the consistent application of the Morison formula for the prediction of the hydrodynamic loads. In contrast to existing methods, the present formulation retains both drag and inertia of the net during this idealization.

Furthermore, the drag resistance of a common purse seine net was measured during towing tank experiments. The examined configuration and the tested speeds correspond to values of the net

solidity and Reynolds number not covered by existing experimental results. Three inclination angles were examined. The obtained drag coefficients were found compatible with predictions of empirical formulae.

The comparison of the results of the finite element model against the measured data revealed the importance of the correct modelling of the shading flow effect, which dominates the hydrodynamic behaviour at large angles of incidence. Pertinent correction factors for the drag coefficient were derived for this case.

The vertical submersion of the seine was examined experimentally (for the early stage of motion) and numerically. For the latter case, an analytical approach was presented and a good agreement between the numerical results and the experimental observations was achieved.

Finally the cyclic deployment of the purse-seine net is simulated. The aim of this analysis was to investigate the diving behavior of the net in the actual fishing conditions and in particular to study the effect of the speed of the skiff on the maximum depth reached by the net during the fishing cycle. It has been identified that for typical skiff speeds the net will reach the sea floor at the early stages of the shooting cycle.

7. Acknowledgements

This work was partly supported by the European Commission and by the Greek Secretariat for Research and Technology.

References

- Aarsnes, J.V., Rudi, H., Løland, G., 1990. Current forces on cage, net deflection, in: Thomas Telford (ed), Engineering for Offshore Fish Farming, London, 137-152.
- Balash, C., Colbourne, B., Bose, N., Raman-Nair, W., 2009. Aquaculture Net Drag Force and Added Mass, Aquacultural Engineering 41, 14-21
- Bathe, K.J., 1996. Finite element procedures. Prentice-Hall, Inc., New Jersey.
- Bessonneau, J.S., Marichal, D., 1998. Study of the dynamics of submerged supple nets (application to trawls). Ocean Engineering 25 (1), 563–583.
- Crisfield, M.A., 1991. Non-linear finite element analysis of solids and structures, Volume 1, John Wiley and Sons, Inc, New York.
- DeCew, J., Tsukrov, I., Risso, A., Swift, M.R., Celikkol, B., 2010. Modeling of dynamic behavior of a single-point moored submersible fish cage under currents, Aquacultural Engineering 43, 38-45.
- European Union, 2006. Council Regulation (EC) No 1967/2006, Official Journal of the European Union, 30/12/2006, L409/11-85.
- Gignoux, H., Messier, R.H., 1999. Computational modelling for fin-fish aquaculture net pens. Oceanic Engineering International, 3 (1), 12-22.
- Haritos, N. and He, D.T., 1992. Modelling the response of cable elements in an ocean environment. Finite Element in Analysis and Design 19, 19-32.
- Huang, C.C., Tang, H.J., Liu, J.Y., 2006. Dynamical analysis of net cage structures for marine aquaculture: Numerical simulation and model testing. Aquaculture Engineering 35, 258-270.
- Katsaounis, G.M., Tzabiras, G., Voutsinas, S.G. and Bergeles, G., 2009. Measurements of drag resistance on purse seine nets with application to their submergence problem. Proceedings of 13th Congress of Intl. Maritime Association of Mediterranean IMAM 2009, Istanbul, Turkey, 12-15 October.
- Kawakami, T., 1959. Development of mechanical studies of fishing gear, in: Modern Fishing Gear of the World, Fishing News (Books), London.
- Kawakami, T., 1964. The theory of designing and testing fishing nets in model, in: Modern Fishing Gear of the World, Fishing News (Books), London.

Lader P.F. and Enerhaug, B., 2005. Experimental investigation of forces and geometry of a net cage in uniform flow. *IEEE Journal of Oceanic Engineering*, vol. 30, no 1, 79-84.

Lader P.F. and Fredheim A., 2006. Dynamic properties of a flexible net sheet in waves and current—A numerical approach. *Aquacultural Engineering* 35, 228–238.

Lee, C.W., Lee, J.H., Cha, B.J., Kim, H.Y., Lee, J.H., 2005. Physical modelling for underwater flexible systems dynamic simulations. *Ocean Engineering*, 32, 331-347.

Lo, A. and Leonard, J.W., 1982. Dynamic analysis of underwater cables. *J. Eng. Mech. Div. ASCE* 108 (EM4), 605-621.

Løland, G., 1993. Current forces on, and water flow through and around, floating fish farms. *Aquaculture International*, 1, 72-89.

Milne, P.H., 1972. *Fish and Shellfish Farming in Coastal Waters*, Fishing News (Books), London.

Morison, J.R, Johnson, J.W, O'Brien, M.P., Schaaf, S.A., 1950. The force exerted by surface waves on piles. *Petroleum Transactions, American Institute of Mining Engineers* 189, 149-154.

Shimizu, T., Tsutomu, T., Holger, K., Tomonori, H., Katsutaro, Y., 2005. Application of NaLA, a fishing net configuration and loading analysis system, to drift gill nets. *Fisheries Research* 76, 67-80.

Stekalova, V.N.. 1964. O Zakone Izmeneniya Sil Soprotivleniya Elementa Trosa (in Russian). *Kaliningradskoe Knizhnoe Izdatel'stvo* 18.

Tsukrov, I., Eroshkin, O., Fredriksson, D., Robinson Swift, M., Celikkol, B., 2003. Finite element modelling of net panels using a consistent net element. *Ocean Engineering* 30, 251-270.

Tsukrov, I., Eroshkin, O., Paul, W. and Celikkol, B., 2005. Numerical Modeling of Nonlinear Elastic Components of Mooring Systems", *IEEE Journal of Oceanic Engineering*, v. 30, No. 1, 37-46.

Tsukrov, I., Drach, A., DeCew, J.C, Swift, M.R., Celikkol, B., 2011. Characterization of geometry and normal drag coefficients of copper nets. *Ocean Engineering* 38, 1979-1988.

White, F., 1974. *Viscous Fluid Flow*. McGraw Hill, pp.182-183.

Zhan J.M., Jia X.P., Li Y.S., Sun M.G., Guo G.X., Hu Y.Z., 2006. Analytical and experimental investigation of drag on nets of fish cages, *Aquacultural Engineering*, 35, 91–101.

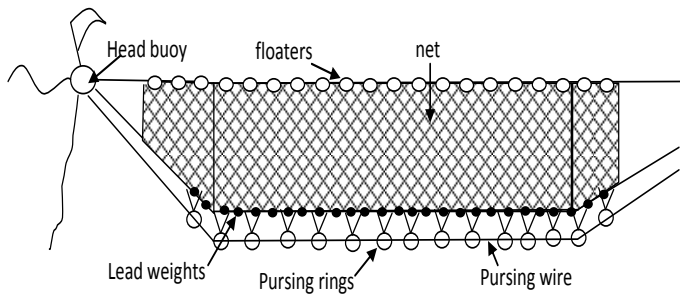


Figure 1: Purse seine components

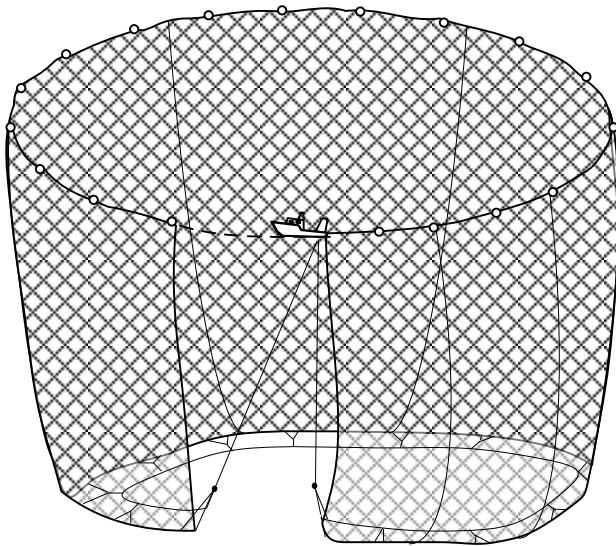


Figure 2: Purse seining (Source: www.eurocbc.org/purseseine.gif)

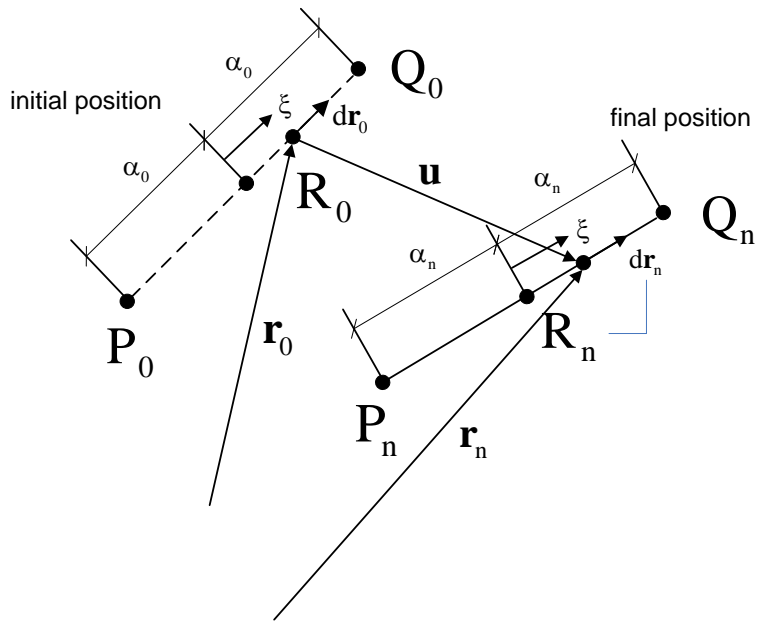


Figure 3: Deformation of a truss element.

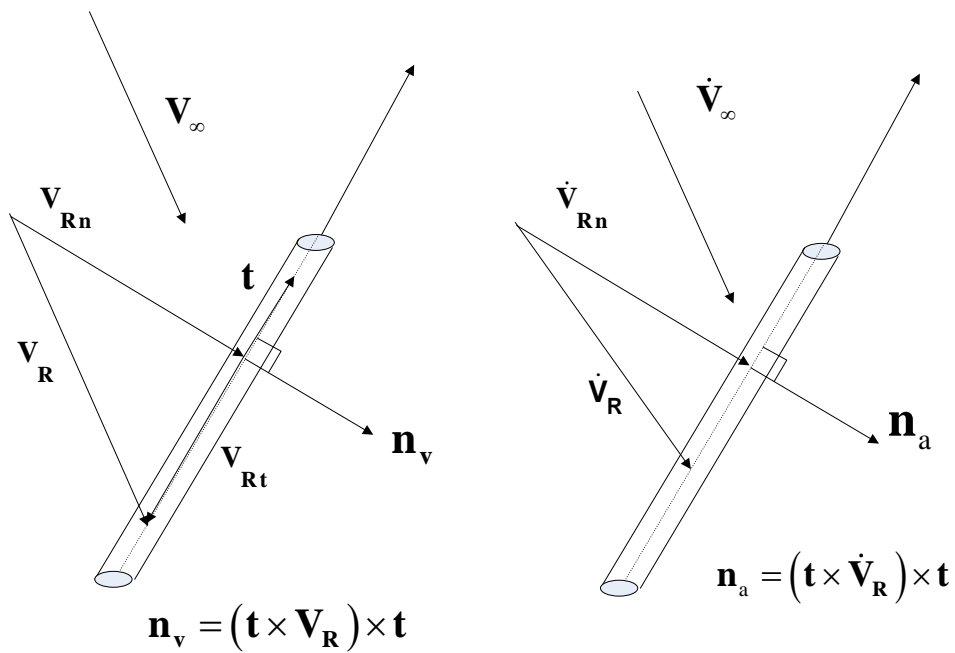


Figure 4: Illustration of relative water velocity and acceleration.

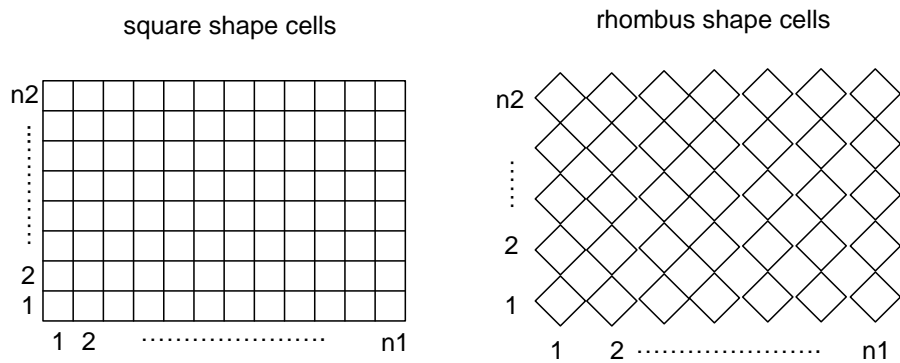


Figure 5: Numbering of the net cells.

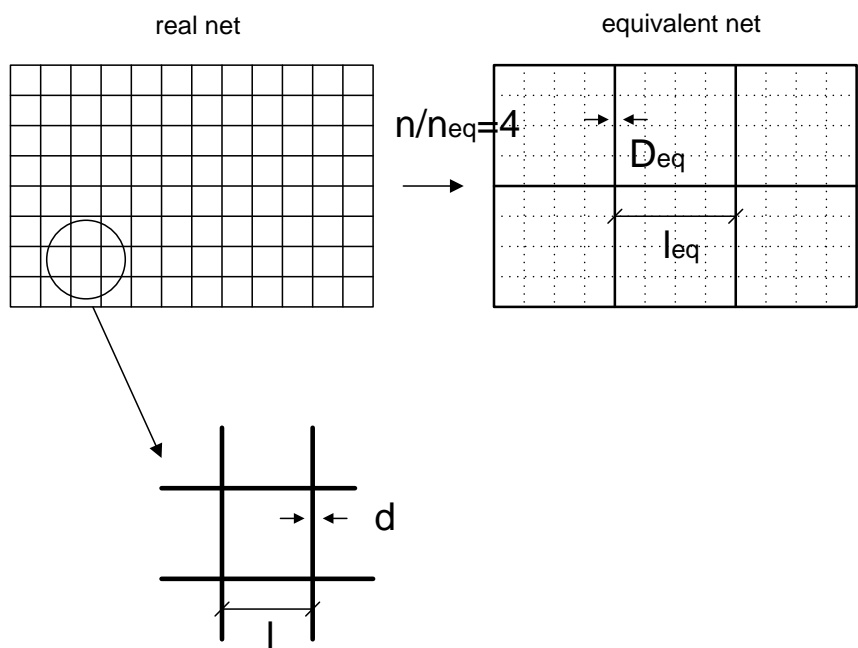


Figure 6: Definition of the equivalent net with a less fine mesh

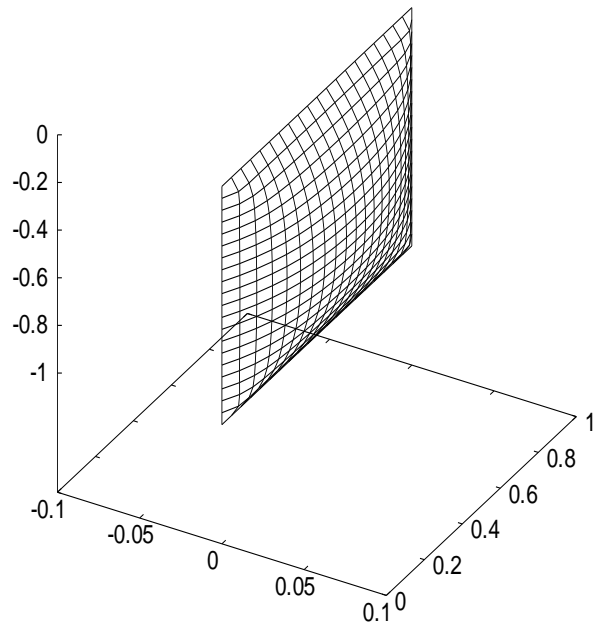


Figure 7: Deformed 1x1 net panel (square type cells) at current velocity 1 m/s

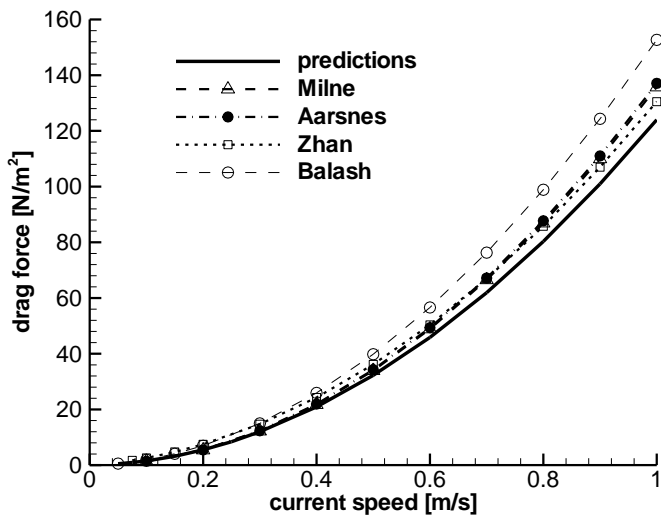


Figure 8: Drag force of net panel with square type mesh as function of the current velocity – comparison with semi-empirical expressions (Reynolds range $35 \div 1400$).

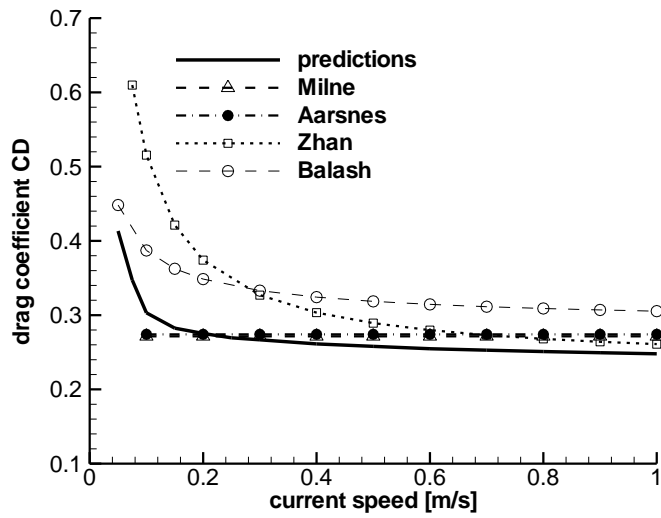


Figure 9: Drag coefficient of net panel with square type mesh as function of the current velocity – comparison with analytical expressions (Reynolds range $35 \div 1400$).

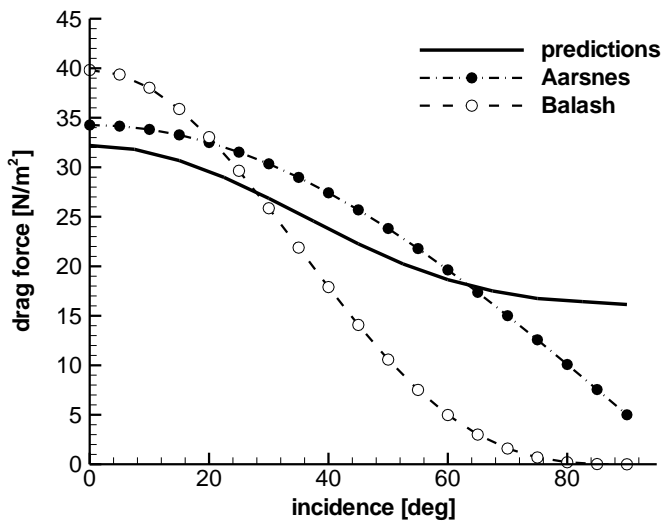


Figure 10: Drag force of net panel with square type mesh as function of the current orientation – comparison with Aarsnes and Balash analytical fomulae ($V = 0.5 \text{ m/s}$, $Re = 700$).

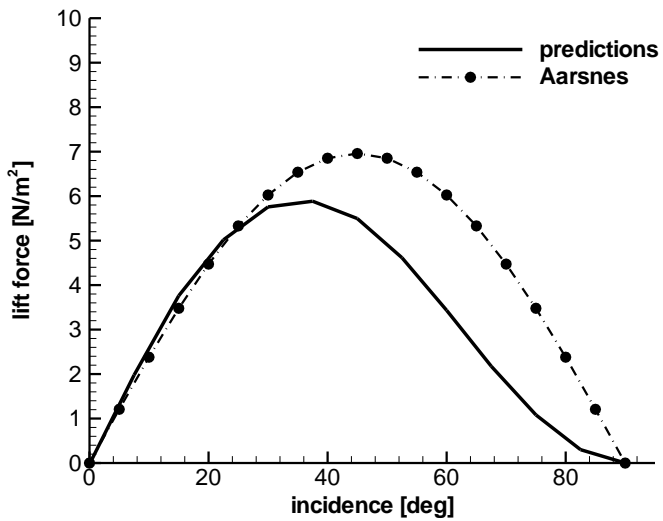


Figure 11: Lift force of net panel with square type mesh as function of the current orientation – comparison with Aarsnes analytical fomula ($V = 0.5 \text{ m/s}$, $Re = 700$).

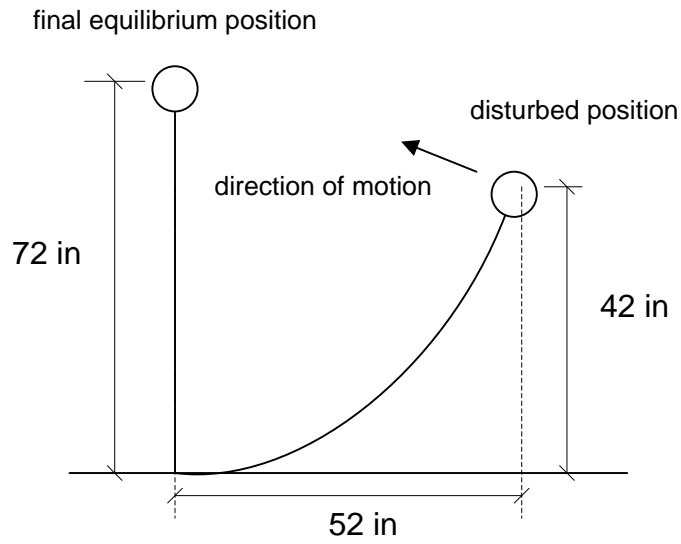


Figure 12: Configuration of single point moored buoy.

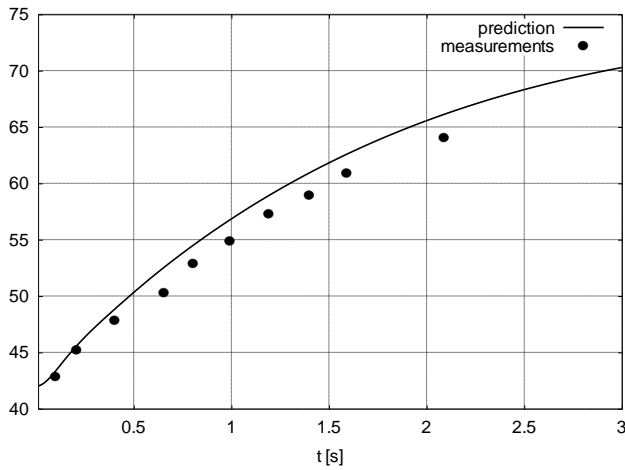


Figure 13: Vertical displacement of moored buoy.

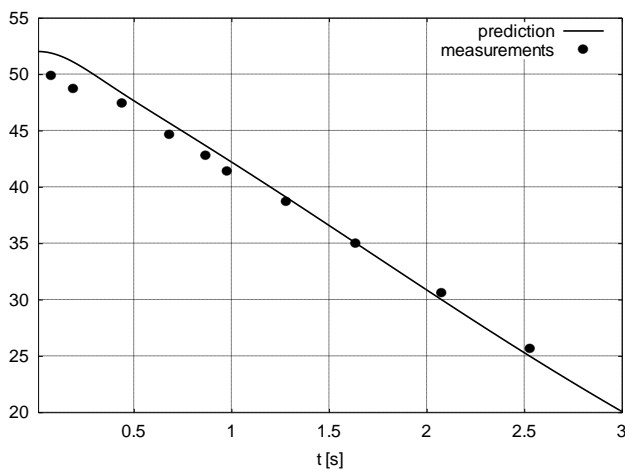


Figure 14: Horizontal displacement of moored buoy.

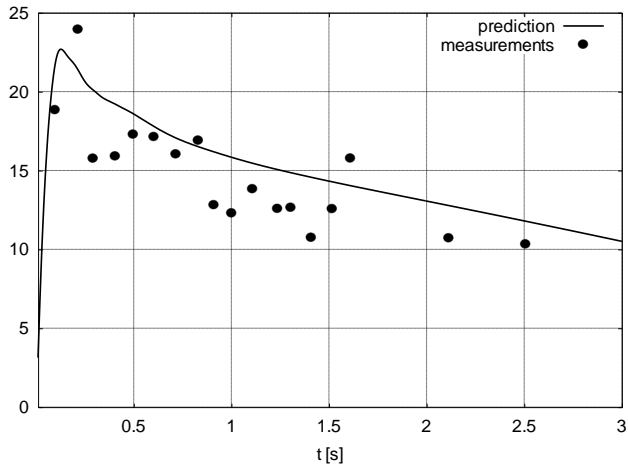


Figure 15: Displacement velocity of moored buoy.

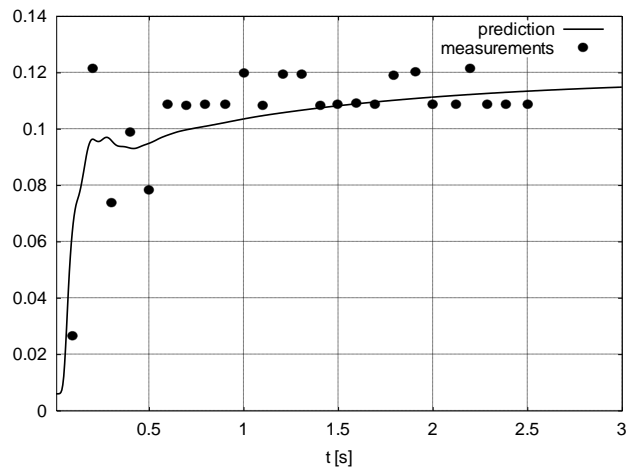


Figure 16: Tension of the cable at the sea bed connection point

cell type	diamond
Seine weight (dry) in air	0.307 N/m ²
Seine weight in water	0.065 N/ m ²
Seine wet mass (inertia)	75.5 gr/m ²
Twine diameter	0.35 mm
Half mesh size	8 mm
Twine material density	1269.54 kg/m ³
Twine material Young's modulus	2x10 ⁹ Pa
Upper and lower rope diameter	6.5 mm
Bottom rope weigh (dry) in air	0.5673 N/m
Bottom rope weigh in water	0.2418 N/m
Bottom rope wet mass (inertia)	135 gr/m
Dimensions of lead weights	Ellipsoids, Ø28mm max. Ø11mm hole Length 33mm Spacing 300mm
Mass of lead weights	100 gr

Table 1: Purse seine net properties.

	$a = n / n_{eq} = 8$	$a = n / n_{eq} = 32$
Equivalent half mesh size	64 mm	256 mm
Equivalent twine diameter (cylindrical twine)	2.8 mm	11.2 mm
Equivalent twine (dry) weight in air	0.00959 N/m	0.03834 N/m
Equivalent twine weight in water	0.00203 N/m	0.00814 N/m
Equivalent wet twine mass (inertia)	2.357 g/m	9.428 g/m
Equivalent twine axial stiffness	1539 N	6158 N

Table 2: Equivalent net properties.

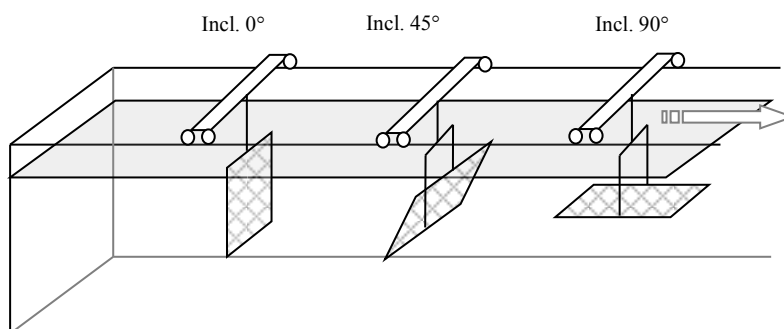
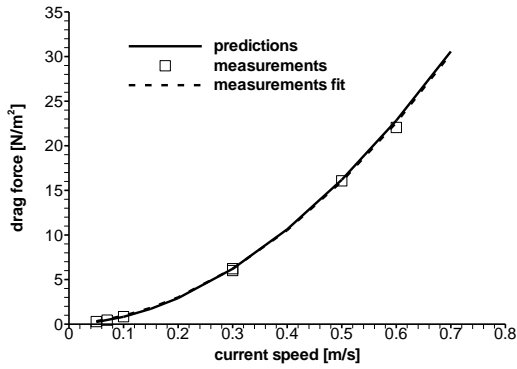
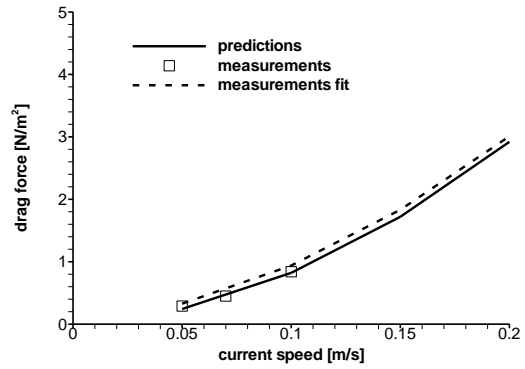


Figure 17: Arrangement for the Resistance tests.

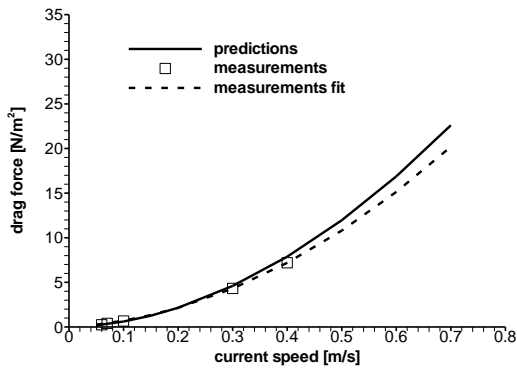


(a)

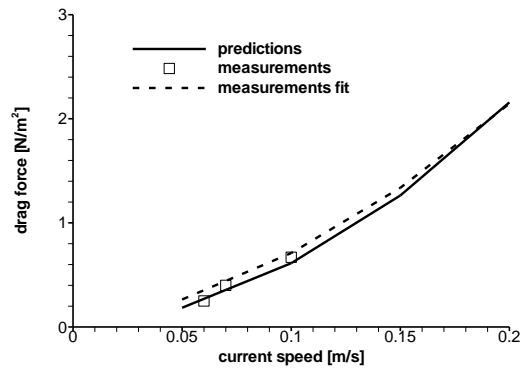


(b)

Figure 18: Drag force on fishing net with diamond type mesh as function of the current speed at $\alpha_w = 0^\circ$ (a) full range (b) focused at low speeds (Reynolds range $15 \div 215$).

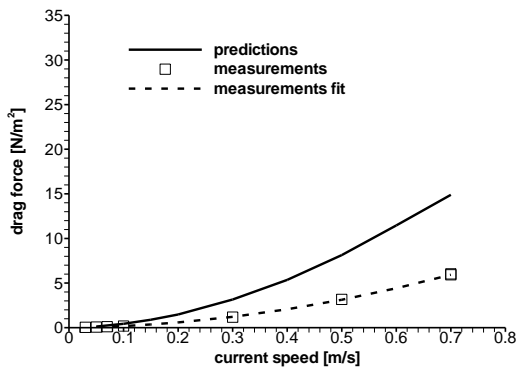


(a)

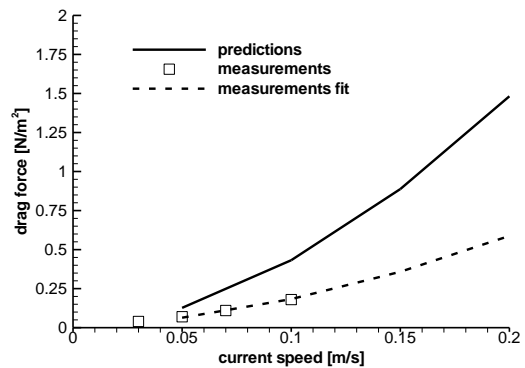


(b)

Figure 19: Drag force on fishing net with diamond type mesh as function of the current speed at $\alpha_w = 45^\circ$ (a) full range (b) focused at low speeds (Reynolds range $15 \div 215$).



(a)



(b)

Figure 20: Drag force on fishing net with diamond type mesh as function of the current speed at $\alpha_w = 90^\circ$ (a) full range (b) focused at low speeds (Reynolds range $15 \div 215$).

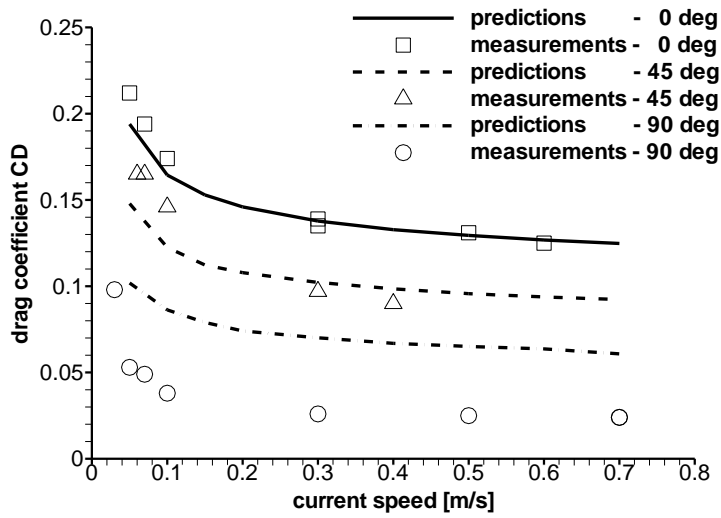


Figure 21: Drag coefficient on fishing net with diamond type mesh as function of the current speed at $\alpha_w = 0^\circ, 45^\circ, 90^\circ$ (Reynolds range $15 \div 215$).

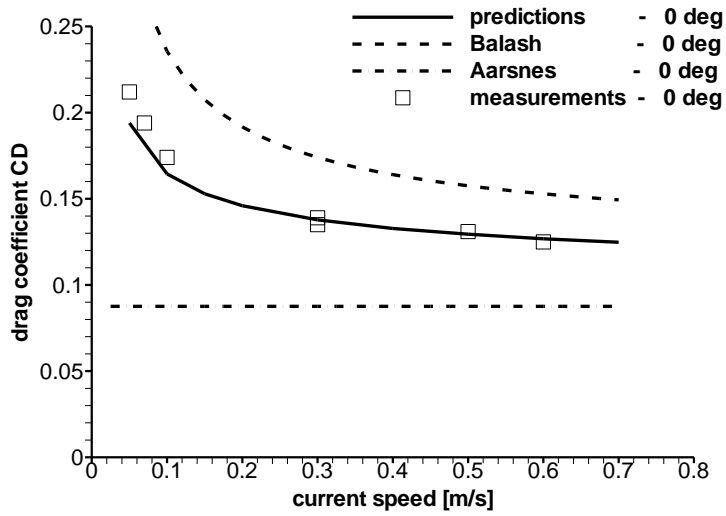


Figure 22: coefficient on fishing net with diamond type mesh as function of the current speed at $\alpha_w = 0^\circ$ comparison against Aarsnes and Balash formulae (Reynolds range $15 \div 215$).

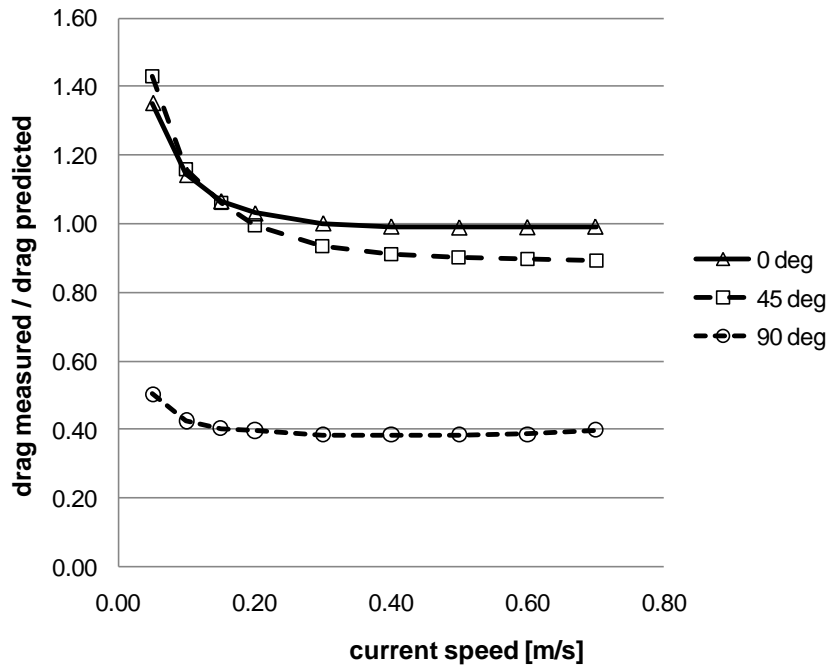


Figure 23: Predicted and measured drag ratio at $\alpha_w = 0^0, 45^0, 90^0$

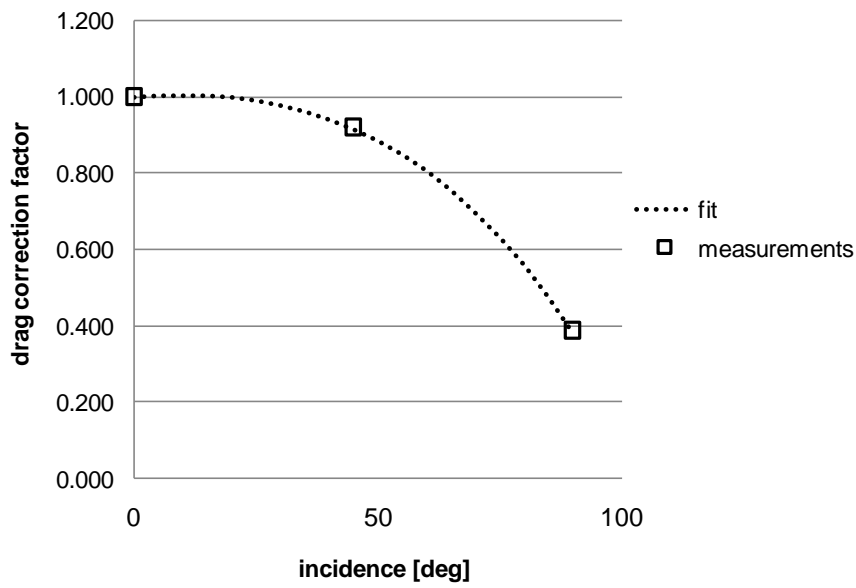


Figure 24: Drag coefficient correction curve.

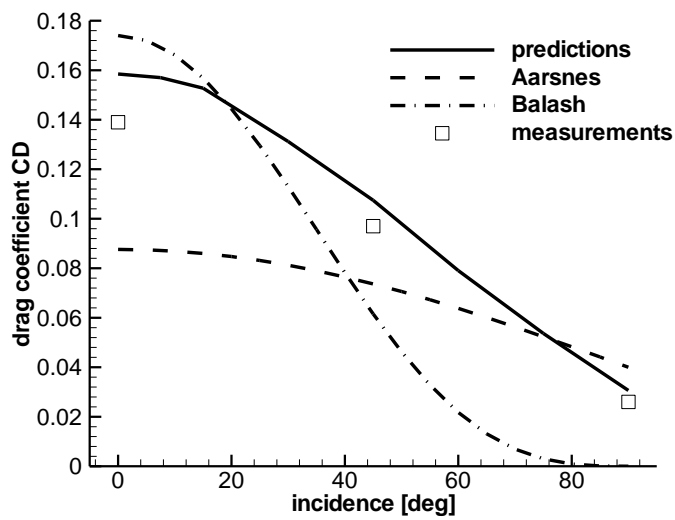


Figure 25: Drag coefficient as function of the current orientation – comparison with Aarsnes and Balash analytical fomulae ($V = 0.3 \text{ m/s}$, $Re = 100$).

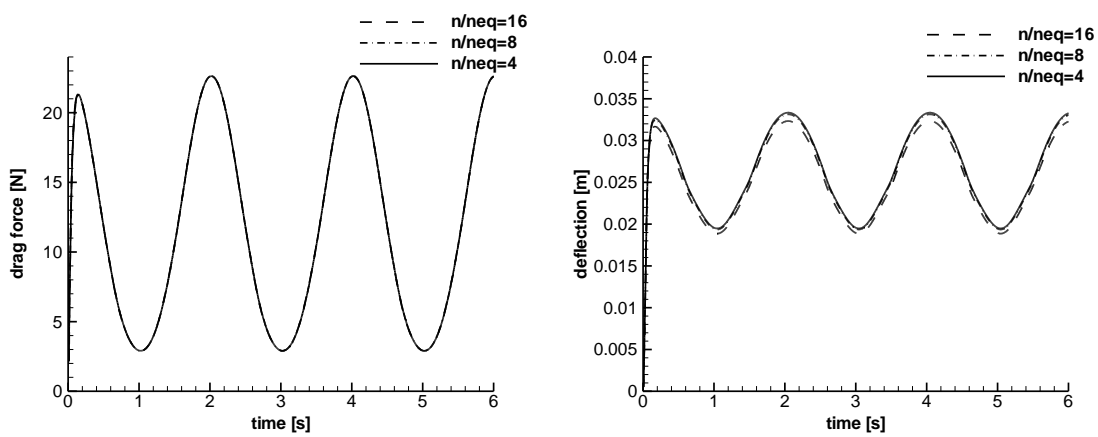


Figure 26: Drag force and net midpoint point deflection in airy wave (wave height $H=0.5 \text{ m}$, wave period $T=2 \text{ s}$)

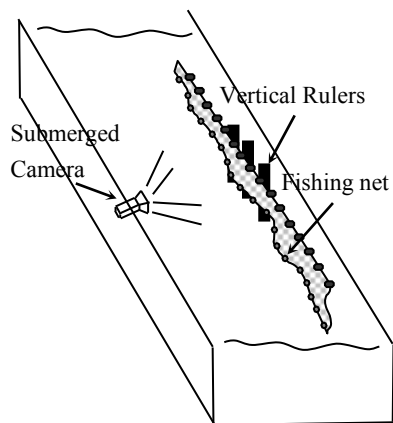


Figure 27: Arrangement for the submergence tests.

Depth (m)	Submersion speed (m/sec)	Time (sec)
1.65	0.5	3.62
2.23	0.25	6.73
2.93	-	9~9.5

Table 3: Purse seine submersion tests

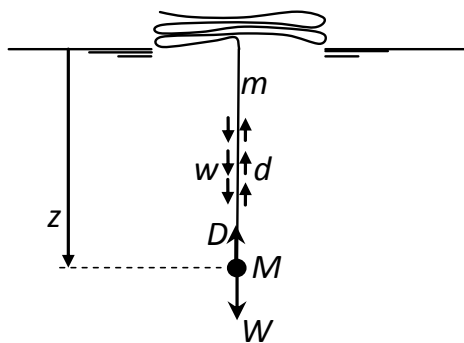


Figure 28: Forces on the free falling net.

Parameter	Value
M	446.7 gr/m
m	75.5 gr/m ²
W	3.173 N/m
w	0.0652 N/m ²

Table 4: Simplified model parameters

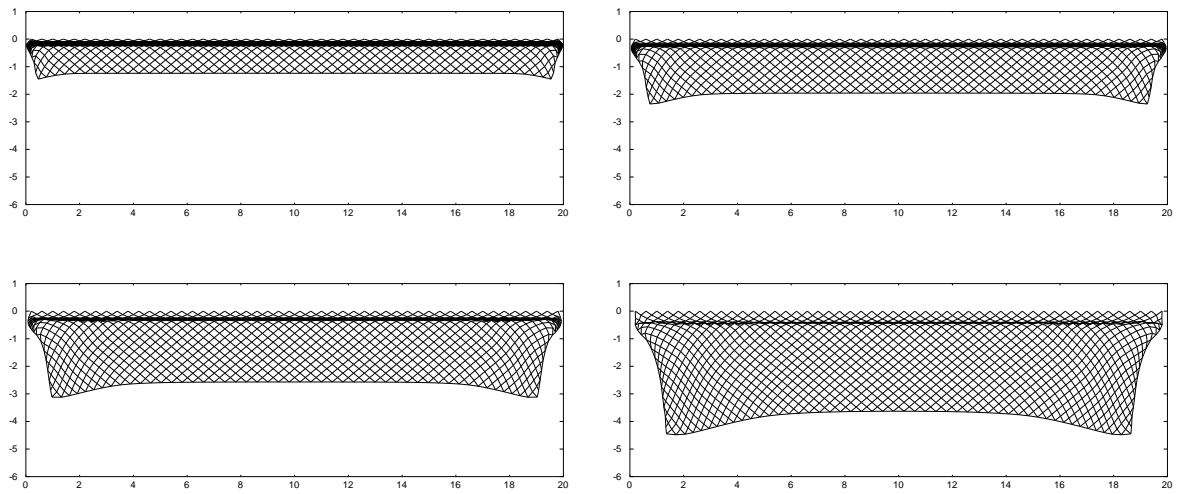


Figure 29: Submerged net geometry at t=2, 4, 6, 10 s

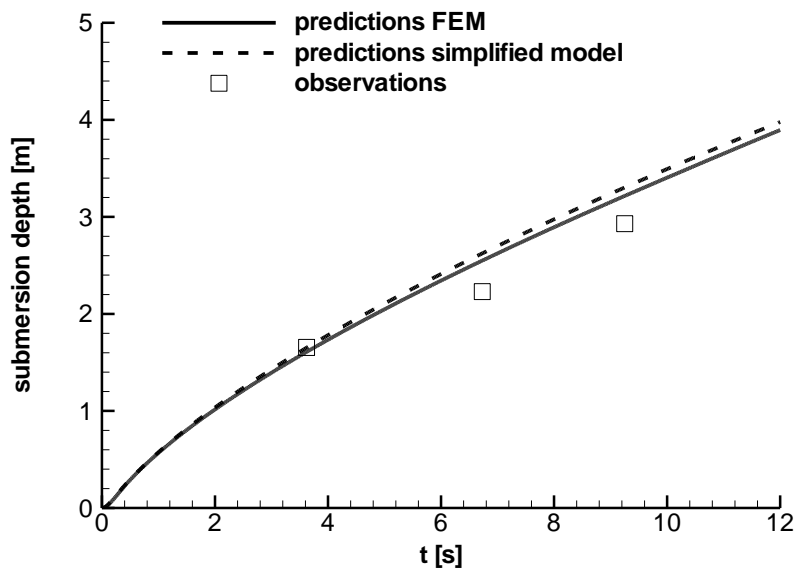


Figure 30: Submersion depth – comparison of measured and predicted data

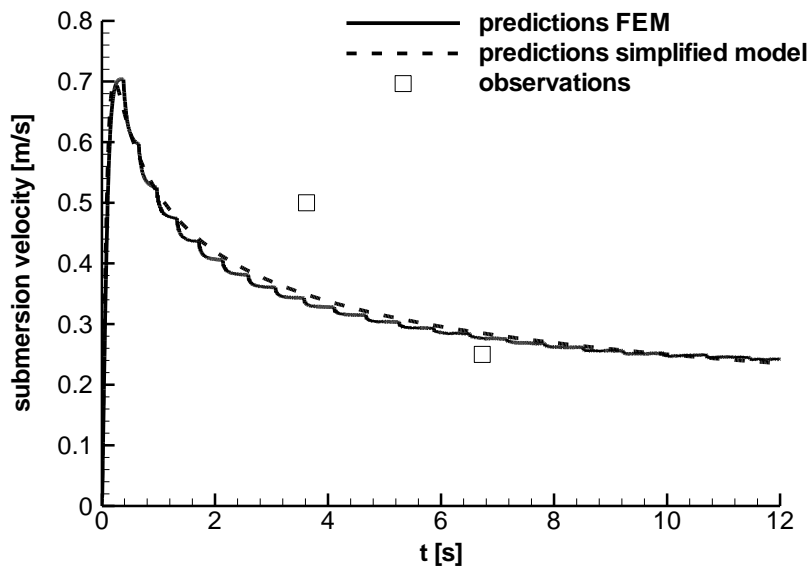


Figure 31: Submersion velocity – comparison of measured and predicted data

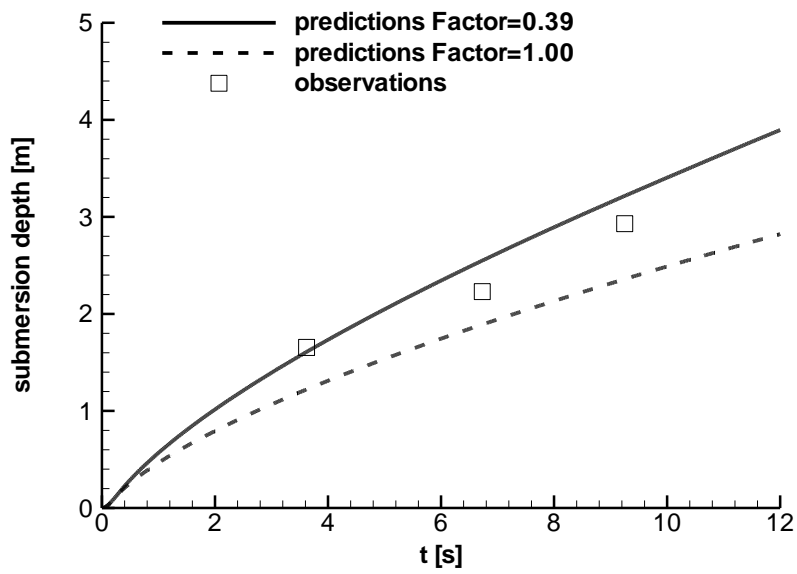


Figure 32: Submersion depth – comparison of measured and predicted data with and without the use of correction factor on the drag.

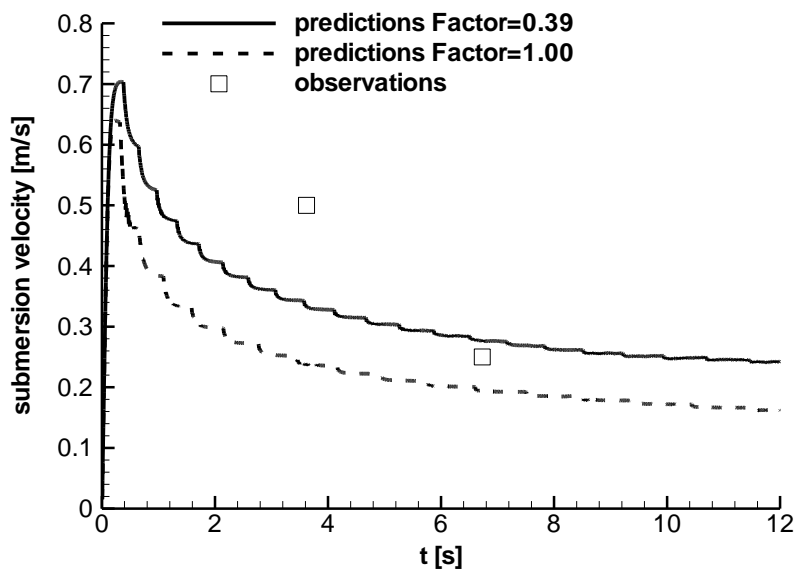


Figure 33: Submersion speed – comparison of measured and predicted data with and without the use of correction factor on the drag.

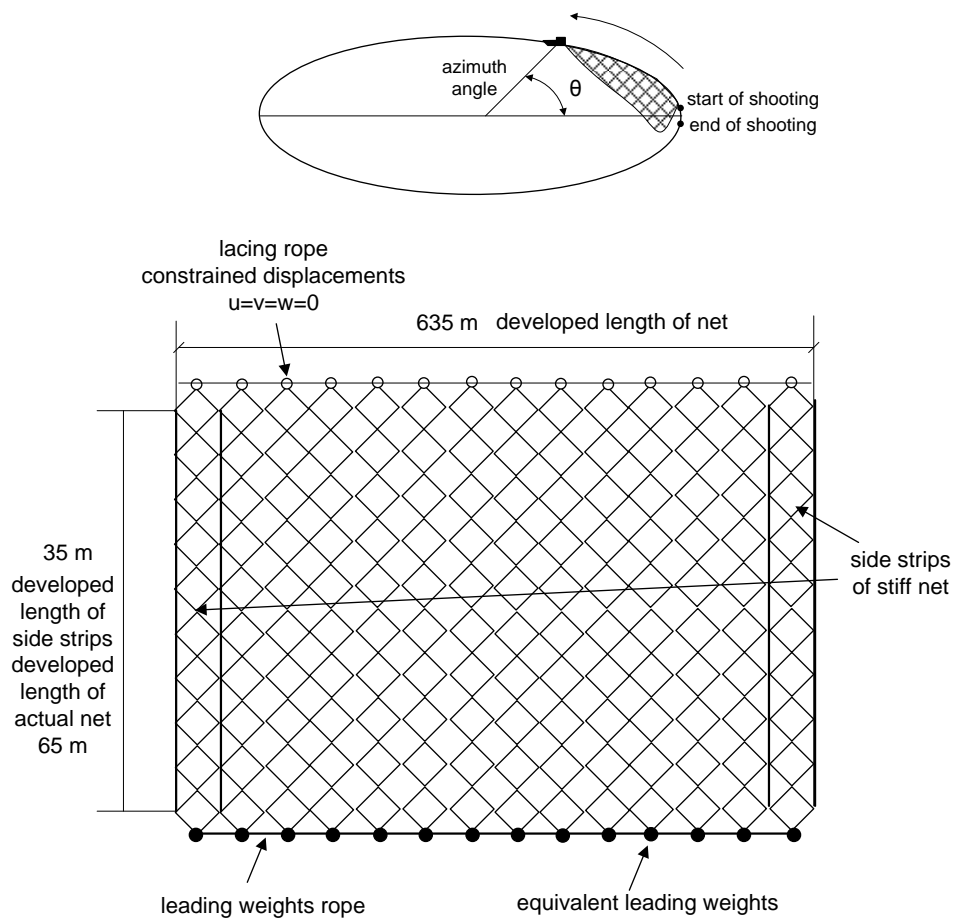
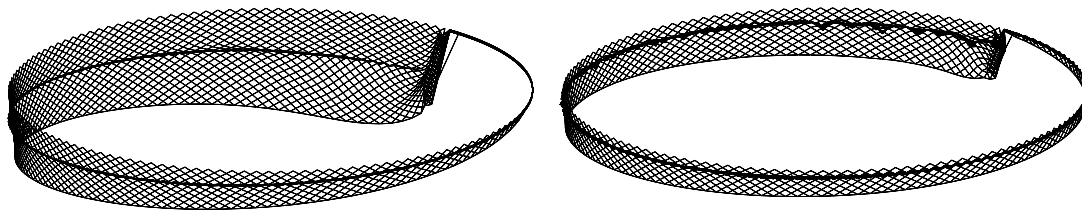


Figure 34: Arrangement of simulated purse seine.



U=1 m/s

U=2 m/s

Figure 35: Snapshot of purse seine submersion for two different speeds of the fishing boat.

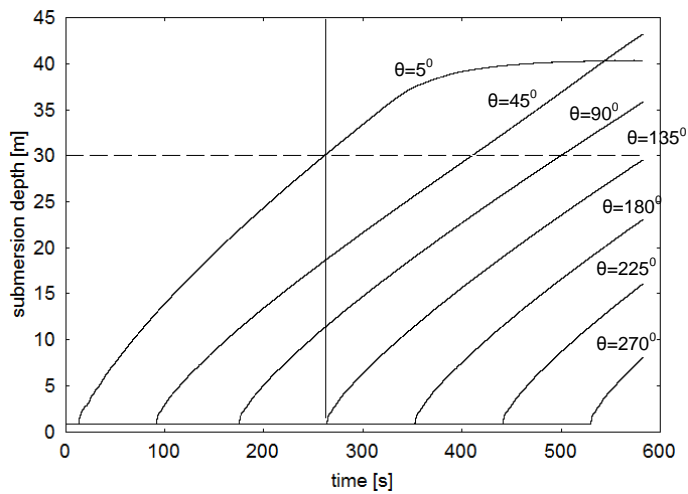


Figure 36: Submersion depth of different points along the circumference of the purse seine (U=1 m/s)

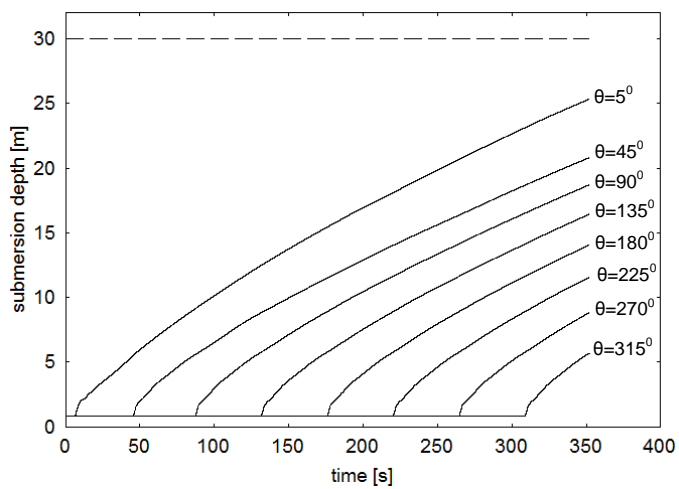


Figure 37: Submersion depth of different points along the circumference of the purse seine (U=2 m/s)

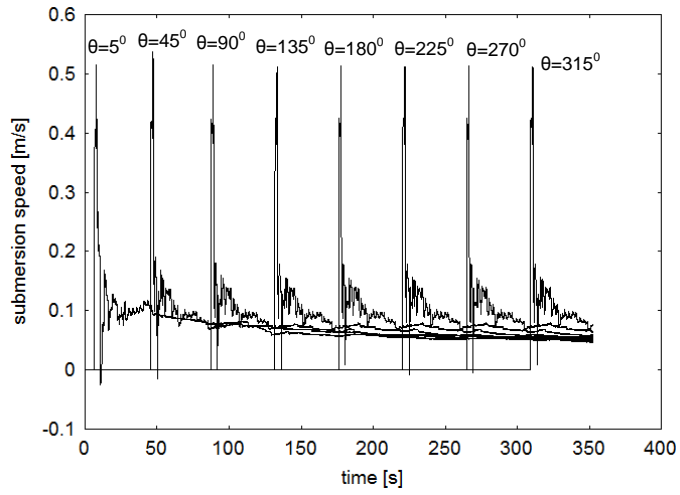


Figure 38: Submersion velocity of different points along the circumference of the purse seine ($U=2$ m/s)